nature portfolio

https://doi.org/10.1038/s41586-026-10968-9

Supplementary information

Foaming photopolymers as a high-resolution biomimetic printing platform

In the format provided by the authors and unedited

Supplementary Information for

Foaming Photopolymers as a High-Resolution Biomimetic Printing Platform

Authors: Detao Qin*[1,2], Xianghui Liu[1,2,3], Baian Kuang[1,2], Yuzhe Zhang[1,2], Masateru Ito[1,2], Tatsuya Katsuno[4], Yuan Liu[1,2,5], Jianduo Zhang[1,2], Claudia Rosa[1,2], Meifang Zhu[5], Mikihito Takenaka[6], Hiroshi Imahori[1,2,7], Ganesh N. Pandian[1,2], Taiki Yanagishima[8,9], Easan Sivaniah*[1,2]

Affiliations:

[1] Institute for Integrated Cell-Material Sciences (iCeMS), Kyoto University, 606-8501, Kyoto, Japan.

[2] Department of Molecular Engineering, Graduate School of Engineering, Kyoto University, 616-8510 Kyoto, Japan

[3] State Key Lab of Metal Matrix Composites, School of Materials Science and Engineering, Shanghai Jiao Tong University, 200240, Shanghai, China

[4] Center for Anatomical Studies, Graduate School of Medicine, Kyoto University, Kyoto 606-8501, Japan

[5] State Key Laboratory of Advanced Fiber Materials, College of Materials Science and Engineering, Donghua University, Shanghai 201620, China.

[6] Institute for Chemical Research, Kyoto University, Gokasho, Uji, 611-0011, Kyoto, Japan

[7] Institute for Liberal Arts and Sciences (ILAS), Kyoto University, Kyoto 606-8316, Japan

[8] Department of Physics, Graduate School of Science, Kyoto University, 606-8502, Kyoto, Japan

[9] Department of Physics, Tokyo Metropolitan University, Hachioji, 192-0397, Tokyo, Japan

*Corresponding authors. Email: qin.detao.8a@kyoto-u.ac.jp, esivaniah@icems.kyoto-u.ac.jp

Table of Contents

Supplementary Note 1

Case-II Diffusion

Method

The diffusion kinetics of the developer (acetic acid) in UV-exposed polystyrene/thioxanthone films was studied in situ using two complementary approaches: confocal laser scanning microscopy (CLSM) and a reflectance measurement.

1. Experimental details of in situ CLSM.

The in situ diffusion of the developer was visualized using a CLSM (Zeiss LSM 880 with Airyscan). The experiment was conducted at room temperature (21±1°C). Here, 4.7-µm-thick polystyrene (192 kDa) films were prepared by spin-casting the solution on cover glass. The photoinitiator (thioxanthone) to polymer ratio was kept at 5 wt%. A fluorescent dye (Rhodamine B, λ_{Ab} max 546 nm, λ_{Em} max 567 nm) was added to the cast solution at 1 wt% to the polymer to facilitate visualization of the polymer film. The films were exposed using Thorlab LEDs (λ_i: 385 nm) for different times to study the effect of energy dosage on diffusion kinetics. CLSM imaging of the polymer layer was performed using a 561 nm excitation laser with a band-pass emission filter of 570–620 nm. A far-red dye (SeTau-647-NHS, λ_{Ab} max 649 nm, λ_{Em} max 695 nm) is optionally added to the developer (acetic acid) and imaged using a 633 nm excitation laser with a 645 nm long-pass filter.

To match the refractive index of the glass, an immersion oil is placed between the objective lens and the cover glass, as shown in the schematic of the experimental setup. The volumetric scanning was started immediately after acetic acid is introduced to the top of the illuminated films. Z-stack scanning was conducted in cycles at fixed time intervals, with the laser switched off after each acquisition for the remainder of the cycle. The Z-stack scanning resolution for film thickness measurements was set to 30 nm, and the lateral (XY) scan area was 10 × 5 µm². An acquisition of a Z-stack scanning typically takes ≥ 30 seconds (single channel).

2. Experimental details of in situ spectrum measurement

The diffusion kinetics of the developer (acetic acid) in UV-exposed polystyrene/thioxanthone films were also investigated by an in situ spectrum measurement. Reflectance spectra were recorded using a UV–vis spectrometer (MCPD-3700, Otsuka Electronics) equipped with a 210–820 nm light source (MC-2530, Otsuka Electronics). Real-time spectral measurements were performed at intervals as short as 0.2 s.

4.7-µm-thick polystyrene (192 kDa) films with 5 wt% thioxanthone were prepared by spin-casting the solution on a glass cover slip. The films were illuminated using Thorlab LEDs (λ_i: 385 nm) for different times to study the effect of energy dosage on diffusion kinetics. The experimental setup is illustrated in Supplementary Fig. 1a: the detector was placed above the glass substrate, while the spin-coated film was located on the underside of the substrate. The setting adopted by this study can significantly improve the quality of the reflectance signal compared to placing the detector above a film supported by a substrate from underneath. Real-time spectra were recorded once development was initiated by injecting acetic acid into the

glass dish containing the sample and sample holder. A hotplate was used to maintain the solvent temperature at a desired value. Measurements were performed at intervals of 0.5 s for 8 min or 0.2 s for 3 min.

A bilayer optical model was built to determine the thickness variation from the in-situ reflectance spectra. As shown in Supplementary Fig. 1b, the model contains a swelling polystyrene layer with a thickness of h_2 and acetic acid fraction of φ_2, and a dense polystyrene layer with a thickness of h_1. The thickness of UV-exposed and developed film are denoted as h_0 and h respectively. A transfer matrix method (TMM) was used to fit the reflectance spectrum using this bilayer model. The thickness of each layer was determined by minimizing the error between the measured and calculated reflectance spectra using an optimization function in MATLAB (version R2024b).

In our model, an intermediate variable Δh_0 is introduced and $h_1 = h_0 - \Delta h_0$. To ensure stable fitting convergence, Δh_0 was constrained to increase monotonically with time, while φ_2 was restricted to the range of 0–1. The three variables, Δh_0, h_2 and φ_2 can be solved with initial value 0. Values are updated iteratively in fitting the in situ spectra, with the output of each step feeding into the next. The refractive index of the swelling layer (n_2) is a combination of the refractive index of polystyrene (n_{PS}) and the refractive index of acetic acid (n_{AA})[1], according to the Lorentz–Lorenz equation[2].

$$n_2 = \sqrt{\frac{1+2\alpha}{1-\alpha}}, \alpha = \varphi_2 \frac{{n_{AA}}^2-1}{{n_{AA}}^2+2} + (1-\varphi_2)\frac{{n_{PS}}^2-1}{{n_{PS}}^2+2} \quad \text{(S1)}$$

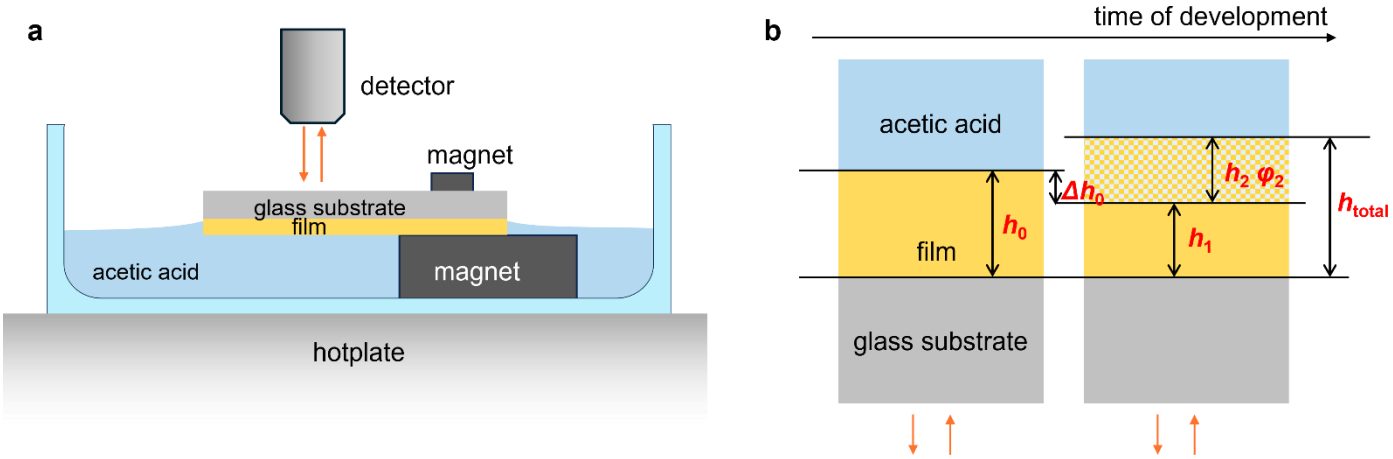

Supplementary Fig. 1 | In situ spectroscopic analysis. **a**, Schematic of the setup of the in-situ spectroscopic measurement. **b**, Schematic of the bilayer optical model used for fitting the in situ reflectance spectra.

Results and discussion

1. Results and discussion of in situ CLSM

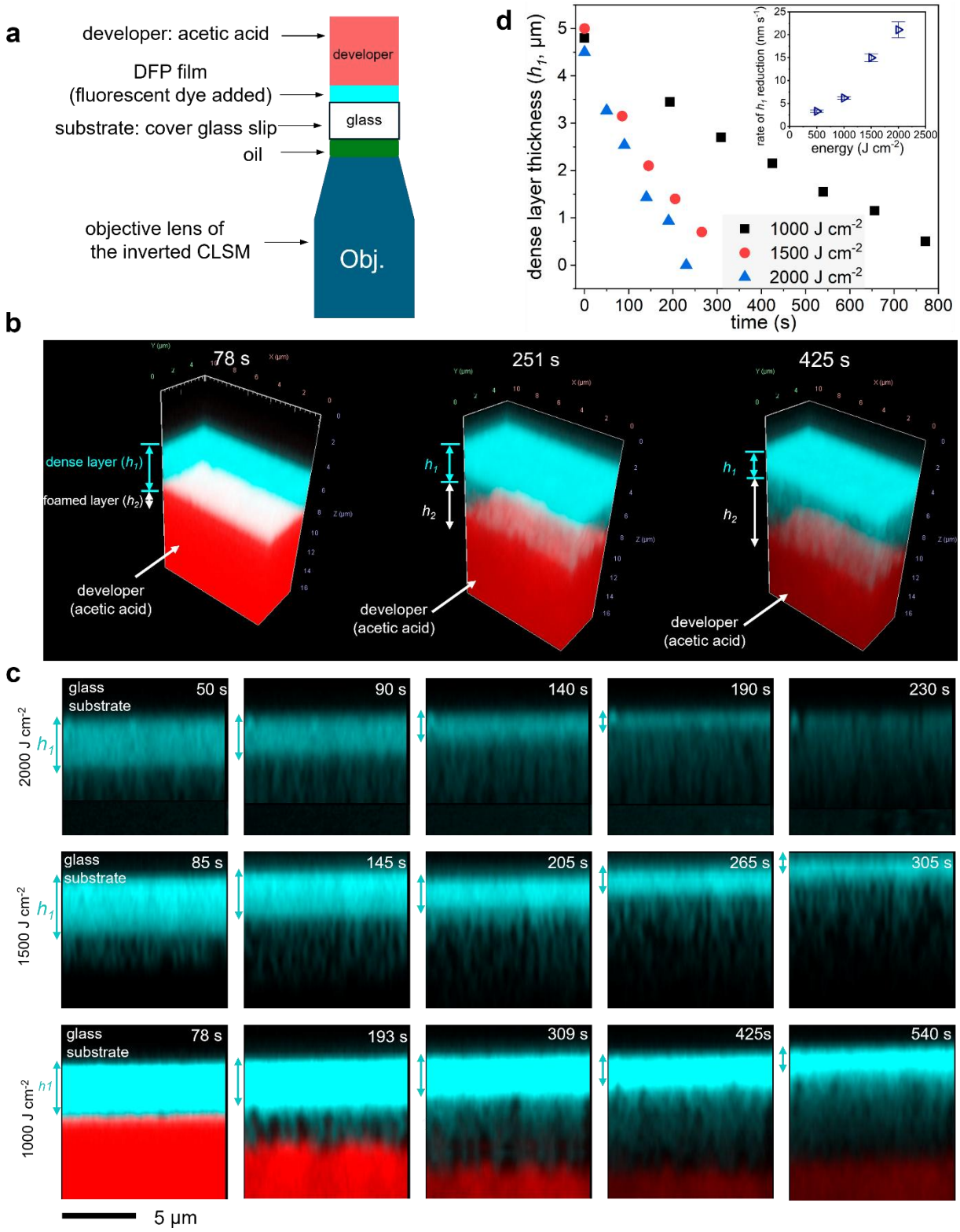

Supplementary Fig. 2 | Visualization of in situ DFP development using a confocal laser scanning microscope (CLSM). **a**, Schematic of the sample configuration on the microscope objective. **b**, 3D reconstruction of in situ DFP development by CLSM (energy dosage: 1000 J cm^{-2}). The thickness of the remaining original layer (h_1) of polymer was tracked to evaluate diffusion kinetics. For visualization purposes, polystyrene film (fluorescence from Rhodamine B) and the developer (acetic acid, fluorescence from SeTau-647-NHS) are pseudo-coloured as turquoise and red respectively. **c**, Side-view CLSM images of in situ development for different energy doses. **d**, Diffusion kinetics based on CLSM. Error bars denote standard deviation (n = 2). Scale bar, 5 μm (**c**).

The schematic of the experimental setup is shown in Supplementary Fig. 2a. The 3D reconstruction of the in situ development is shown in Supplementary Fig. 2b. The Z-stack scanning reveals a clear diffusion boundary (a key feature of Case II diffusion) and tracks its propagation through the dense layer of the film. The remaining thickness of the original dense layer (h_1, the same label as in situ spectrum measurement) was monitored to study the diffusion kinetics. However, it is worth noting that in situ pore growth also generates a strong scattering effect, which limits penetration of the laser beam (typically ≤10 μm from the glass-film interface). Therefore, the foamed layer (h_2, the same label as in situ spectrum measurement) cannot be fully tracked by CLSM, as the growth and coalescence of pores continue in the region beyond the effective laser detection length. A far-red fluorescent dye (SeTau-647-NHS, λ_{Ab} max 649 nm, λ_{Em} max 695 nm) can be added in the developer to assist the CLSM visualization. It should also be noted that sequential scanning of the two fluorophores utilizing two separate channels results in a two-fold increase in the acquisition time.

Supplementary Fig. 2c presents side-view CLSM images for films illuminated with different energy dosage for comparison. Supplementary Fig. 2d summarizes the diffusion kinetics based on the CLSM study: for DFP films exposed to an energy dosage of 1000–2000 J cm^{-2}, the dense layer thickness was "consumed" at a linear speed by acetic acid diffusion at room temperature. This evidences case-II diffusion during solvent permeation at the beginning of the DFP process. Moreover, the diffusion speed (rate of h_1 reduction) is increased with energy dosage. The higher diffusion speed can be attributed to more chain scission products generated by a higher energy dosage, as indicated by the GPC and FTIR study, which enhances the interaction between polymer and developer, and drives faster diffusion in the film.

2. Results and discussion of in situ spectrum measurement

The overall growth of the film thickness at early times is the time-integrated result of migration of the solvent diffusion front nucleating new bubbles, and the subsequent growth of these individual bubbles. Tracing the dynamics of each of these processes is essential to understanding the growth dynamics of the foam. Thus, we used a bilayer model which showed excellent agreement with experimental reflectance data, as shown in Supplementary Fig. 3a, to trace the change in layer thicknesses (h_1, h_2, h) and the fraction of acetic acid (φ_2) in the solvent infiltrated layer, as shown in Supplementary Fig. 3b. We find that the change of h_1, corresponding to solvent front migration in the film, varies linearly with development time. Thus, we may conclude that this solvent migration follows case II diffusion. Supplementary Fig. 3c plots h_1 versus development time for films with different energy dosages. Supplementary Fig. 3d shows that rate of h_1 reduction depends on UV energy dosage, molecular weight of polymer, and development temperature. For both 192-kDa and 35-kDa polystyrene, diffusion speed (rate of h_1 reduction) is increased with energy dosage. As supported by the GPC and FTIR studies, a higher energy dosage generates more chain scission and oxidized functional groups, which enhances the affinity of the polymer film to acetic acid and hence accelerates the diffusion.

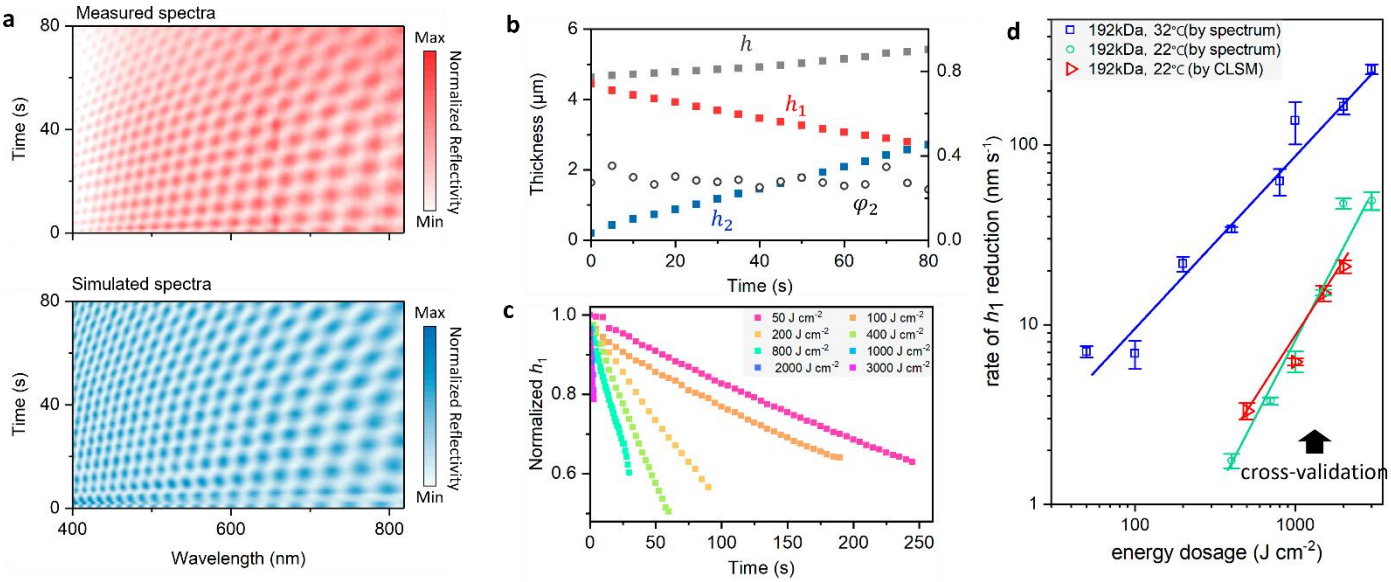

Supplementary Fig. 3 | Spectroscopic analysis of in situ DFP development. a, Examples of the measured and simulated spectra. **b**, Change in film thickness and acetic acid fraction over development time. In (**a**) and (**b**) 192-kDa polystyrene films were exposed to the Thorlabs LEDs (λ_i: 385 nm) at an energy dose of 200 J cm^{-2} and then developed in 32 °C acetic acid. **c**, Dense layer thickness (h_1) versus development time for 192-kDa polystyrene film with different energy dosage. Development temperature is 32°C. **d**, Cross-validation of h_1 reduction rate by both in situ spectroscopic analysis and CLSM measurement. Lines are drawn as a guide to the eye. Error bars denote standard deviation (n = 2).

Meanwhile, it should be noted that the fitting results represent only the early stage of the development process. We note that the time scales over which such fitting is possible depends on experimental conditions. For example, for a higher molecular weight polystyrene (192 ka), effective spectral variations can be recorded over an extended period for film received a lower energy dosage (Supplementary Fig. 4a). This is because solvent-induced phase separation, pore formation and growth are generally slower in speed. On the contrary, for the film received a higher energy dosage, or developed at a higher temperature, pore formation and growth occur soon after introducing the acetic acid. The film can be developed even by the acetic acid vapor before the solvent touches the surface. Hence the reflectance signal becomes featureless quickly, which does not support the reliable fitting over an extended time (Supplementary Fig. 4b). In addition, we note that the time at which the solvent is introduced to the film surface can be identified by a sharp intensity drop in the real-time reflectance spectra.

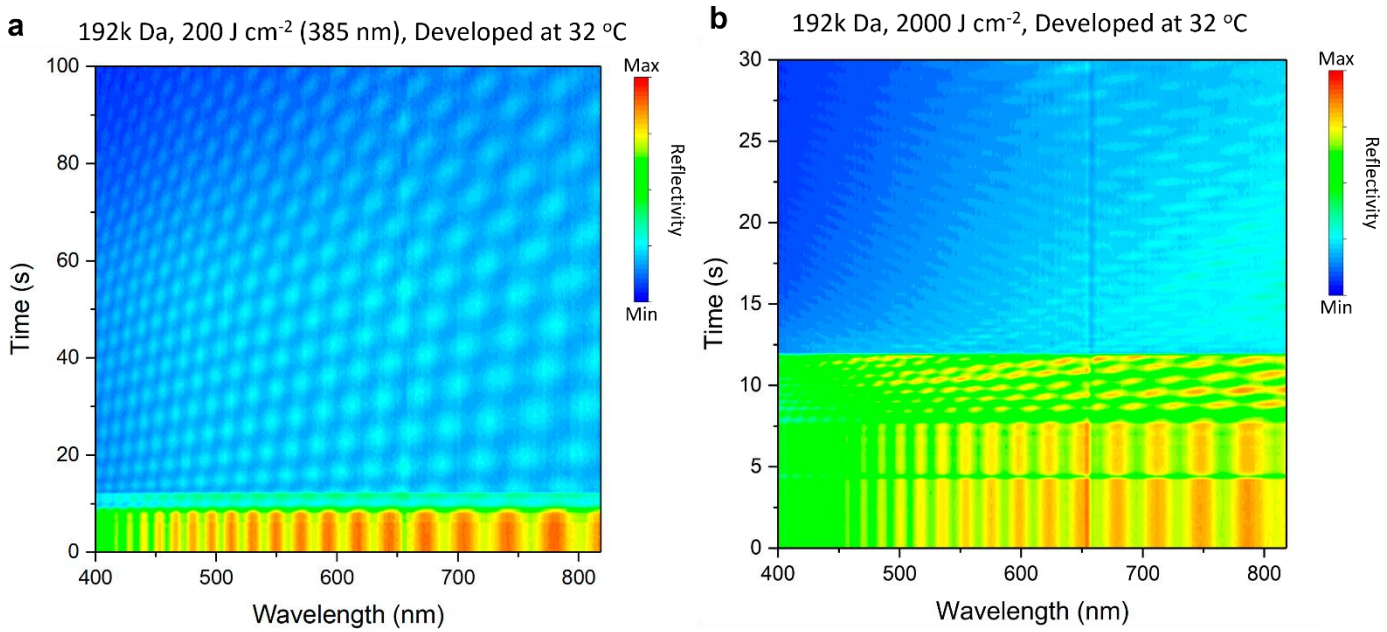

Supplementary Fig. 4 | Example of reflectance spectra measured in situ. **a**, Effective spectral fitting over an extended experimental time is achieved for 192-kDa PS with a lower energy dose (200 J cm^{-2}, developed in 32°C acetic acid). **b**, Effective time window for spectral fitting becomes shorter for a 192-kDa PS with a higher energy dose (2000 J cm^{-2}, developed in 32°C acetic acid).

3. Cross-validation of in situ CLSM and spectroscopic analysis

The two studies of in situ diffusion above were directly compared, adopting the identical experimental conditions: 192-kDa polystyrene, UV energy dosage of 400–3000 J cm^{-2}, and developed in 22°C acetic acid. The results are plotted as green circles and red triangles in Supplementary Fig. 3d for spectroscopic analysis and CLSM, respectively. There is good agreement in the diffusion kinetics measured by the two approaches. Cross-validation using two independent experimental strategies reinforces the credibility of our findings.

Supplementary Note 2

Photochemical Mechanism of Deepfoam Photolithography (DFP)

Method

1. Contrast curve measurement

Contrast curves were used to evaluate the photosensitivity of the polymer films by correlating vacuum-dried thickness of the developed films to UV energy dosage. Polymer films were prepared by spin-casting PS (M_w: 192 kDa and 35 kDa) solutions containing thioxanthone (THX) at concentrations of 1–15 wt% relative to PS content. The as-cast films had an initial thickness of 4.7 ± 0.2 μm. The films were irradiated using a custom LED chamber (Thorlabs: λ_i: 385 nm) with energy dose ranging from 50 to 3000 J cm^{-2}. After exposure, the films were developed in acetic acid at 32 ± 1 °C for 10 min to selectively remove photoinduced chain-scission products. The developed films were then dried under vacuum at 180 °C for 2 h to remove residual solvent and collapse internal porosity, yielding dense polymer films.

Film thicknesses were measured using a surface profiler (DektakXT, Bruker). The vacuum-dried thickness is normalized by as-cast thickness and plotted as a function of energy dose to generate the equivalent of a photoresist-like contrast curve.

2. Thermogravimetric analysis (TGA)

Thermogravimetric analysis (Shimadzu DTG-60) was performed to assess the thermal stability of the polymer after UV irradiation. Polymer films were prepared from solutions containing 6.5 wt% PS (M_w: 192 kDa) and 5 wt% THX (relative to PS) using the same fabrication procedure described above, yielding films with an initial thickness of 4.7 ± 0.2 μm. The films were irradiated with a 385 nm LED light source for energy dose of 100–3000 J cm^{-2}.

After irradiation, the films were dissolved in chloroform, and the solvent was evaporated to obtain the corresponding polymer residues. The residues were further dried under vacuum at 80 °C overnight to ensure complete removal of chloroform before TGA measurement.

TGA was conducted under a nitrogen atmosphere. Samples were equilibrated at 25 °C for 30 min prior to heating to ensure complete purging. The temperature was then increased from 25 to 800 °C at a rate of 10 °C·min^{-1}, and the weight loss was recorded as a function of temperature.

3. Attenuated total reflection Fourier transform infrared (ATR-FTIR) spectroscopy

ATR-FTIR spectroscopy (NICOLET iS50) was used to probe chemical changes in the polymer induced by UV irradiation. Polymer samples were prepared following the same procedure as those used for TGA measurements.

ATR-FTIR spectra were collected at room temperature using an ATR crystal, with 128 scans accumulated for each measurement. All spectra were baseline-corrected, and changes in absorption bands were analysed to identify UV-induced modifications of functional groups.

4. Gel permeation chromatography (GPC) measurement

GPC was employed to evaluate the molecular-weight evolution of the polymers after UV irradiation. Polymer films were prepared as described above and dissolved in tetrahydrofuran (THF) after exposure. For each measurement, a single film cast on a glass substrate (2.4 cm × 2.4 cm) was dissolved in 3 mL of THF, and the solution was filtered through a 0.45 μm syringe filter prior to injection.

GPC measurements were performed using a standard system equipped with column (Shim-pack GPC-80M), operated at 30 °C with a flow rate of 1.0 mL·min^{-1}, using THF as the eluent. Number-average (M_n) and weight-average (M_w) molecular weights were determined by calibration with polystyrene standards.

5. Quantification of chain scission parameters

The average number of chain scissions per macromolecule (S) and the number of scission events per unit mass (N_s) were calculated from the GPC-derived M_n values. The parameter S was defined as

$$S = \frac{M_{n,0}}{M_{n,t}} - 1 \tag{S2}$$

where $M_{n,0}$ and $M_{n,t}$ denote the number-average molecular weights before and after UV irradiation, respectively.

The number of scission events per unit mass, N_s, was calculated according to

$$N_S = \frac{1}{M_{n,t}} - \frac{1}{M_{n,0}} \tag{S3}$$

All scission parameters were derived from the soluble polymer fraction accessible by GPC analysis.

Results and Discussion

Supplementary Fig. 5 correlates the contrast curves of the PS/THX system with molecular-weight evolution and thermal stability, providing insight into the chemical states governing foam formation. In contrast to chemically amplified photoresists, which exhibit a sharp dissolution threshold arising from cooperative deprotection reactions, the present system shows a gradual, dose-dependent decrease in the insoluble fraction. This behaviour reflects a polymer-dominated response governed by the competition between chain scission and crosslinking.

As shown in Supplementary Fig. 5a, the remaining fraction decreases continuously with increasing exposure dose, consistent with progressive photoinduced scission of the PS backbone. The absence of a well-defined dissolution threshold indicates that solubility is dictated by the statistical accumulation of bond-cleavage events rather than by a single critical chemical transformation. Notably, the contrast curves converge to a finite residual fraction at long exposure times, implying the formation of an insoluble network that persists despite extensive degradation.

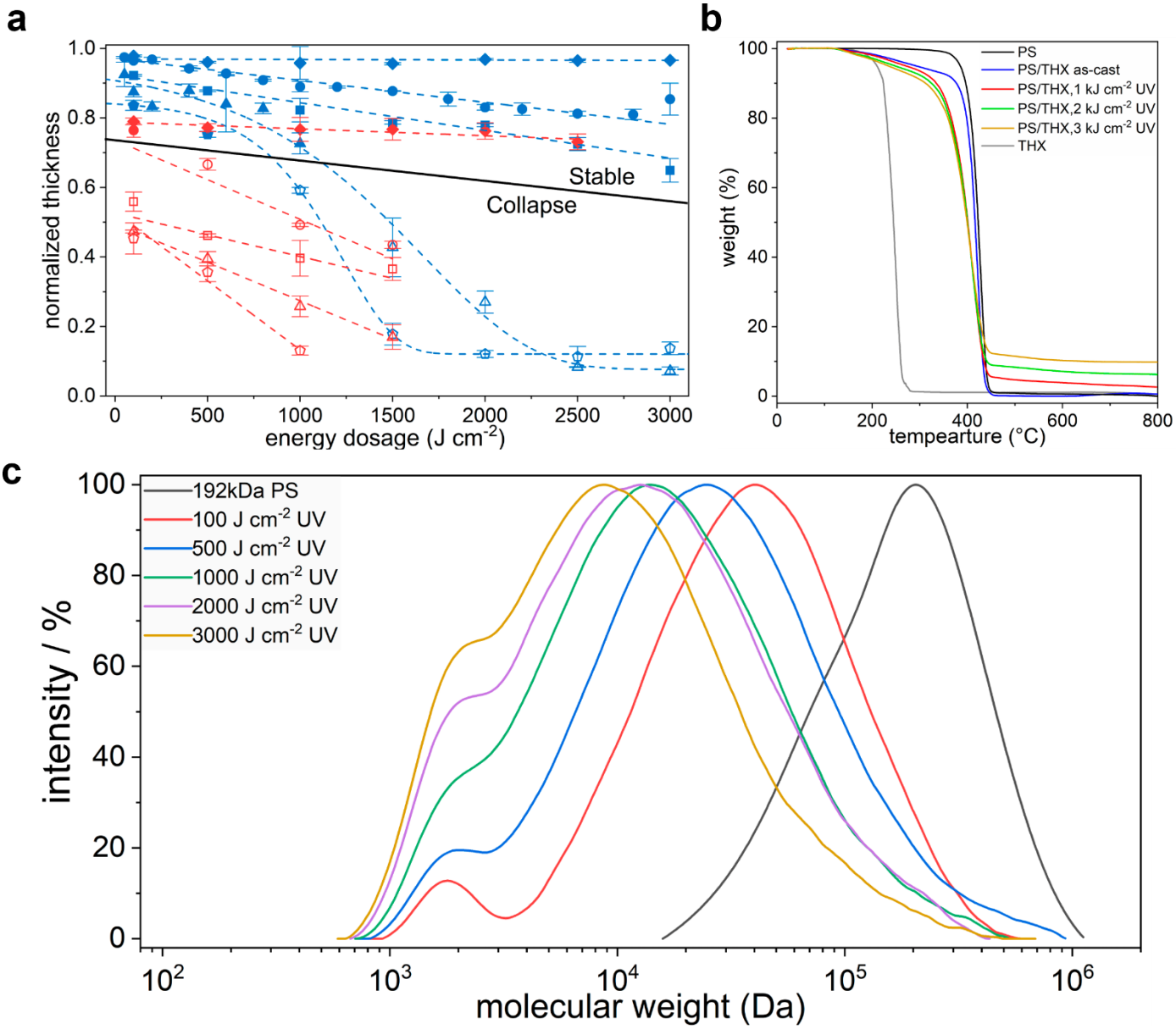

Supplementary Fig. 5 | Contrast curves, TGA and GPC analysis. a, Contrast curves of 192-kDa (blue symbols) and 35-kDa (red symbols) PS films. For 192-kDa PS films, diamonds, circles, squares, triangles, and pentagons denote THX-to-PS ratios of 2.5 wt%, 5 wt%, 7.5 wt%, 10 wt%, and 15 wt% respectively. For 35-kDa PS films, diamonds, circles, squares, triangles, and pentagons denote THX-to-PS ratios of 1 wt%, 5 wt%, 7.5 wt%, 10 wt%, and 15 wt% respectively. The DFP films were developed in 32°C acetic acid for 10 min. Solid and open symbols denote stable growth and collapse, respectively, and lines are drawn as a guide to the eye. Error bars denote standard deviation (n = 2). **b**, Thermogravimetric analysis (TGA) of 192-kDa PS films containing 5wt% THX under different UV exposure dosage. **c**, Gel permeation chromatography (GPC) traces of 192-kDa PS films with 5wt% THX under varying UV exposure dosage.

The shape of the contrast curves is strongly dependent on the THX concentration, which modulates the balance between chain scission and network formation. At low THX loading (1 wt% and 2.5wt%), the remaining fraction is only weakly dependent on exposure dose, indicating that chain scission is insufficient to disrupt network integrity. At high THX loading (10wt% and 15wt%), a rapid loss of material is observed at intermediate doses, followed by a small residual fraction, consistent with excessive degradation of the structural backbone. In contrast, an intermediate THX concentration (5wt%) produces a gradual yet

controlled decrease in the remaining fraction together with a stable insoluble residue, defining a regime in which solubilization and network formation coexist.

This interpretation is supported by GPC analysis (Supplementary Fig. 5c), which shows a systematic shift of the molecular-weight distribution toward lower values with increasing exposure, directly evidencing progressive chain scission.

Quantitatively, M_w exhibits a pronounced decrease at early exposure doses, whereas the calculated chain scission parameters S and N_s increase monotonically with continued irradiation (Supplementary Table 1). As further illustrated in Supplementary Fig. 6, the decrease in M_w closely parallels the monotonic increase in N_s over the entire exposure range. This comparison highlights an apparent discrepancy between molecular-weight evolution and the near-linear decay observed in the contrast curves. The origin of this difference lies in the distinct physical meanings of the observables: M_w is highly sensitive to the first few chain scission events, such that a small increase in the average number of scissions per chain leads to a pronounced reduction in M_w. In contrast, the remaining fraction reflects a macroscopic, cumulative response to degradation and therefore correlates more closely with the steady increase in the average number of chain scissions (S) and the number of scission events per unit mass (N_s). Consistently, both S and N_s increase monotonically with exposure dose (Supplementary Table 1), supporting a statistical scission process within the extractable polymer fraction probed by GPC.

Supplementary Table 1 | Average molar mass (M_w), average chain scissions (S) and number of chain scission events (N_s) of PS/THX Samples under different energy doses.

Sample	Energy dose (J cm^{-2})	M_w (Da)	M_n (Da)	S	N_s (10^{-5} mol g^{-1})
PS/THX	0	224201	125678	0	0
	100	63000	20260	5.20	4.14
	500	55958	13511	8.30	6.61
	1000	34262	8734	13.4	10.7
	2000	30783	7297	16.2	12.9
	3000	23591	5853	20.5	16.3

The absence of high-molecular-weight species in the GPC traces does not preclude crosslinking; rather, crosslinked structures formed upon irradiation are insoluble and are therefore removed during sample preparation, rendering them inaccessible to conventional GPC analysis. Complementary evidence is provided by thermogravimetric analysis (Supplementary Fig. 5b). Upon irradiation, the PS/THX samples exhibit increased mass loss at lower temperatures relative to pristine PS, with the effect becoming more pronounced at longer exposure times, consistent with the formation of lower-molecular-weight fragments. Simultaneously, the emergence and growth of a high-temperature residue indicate the formation of a thermally stable, insoluble network. Together, these results demonstrate that the gradual decay and finite residual fraction observed in the contrast curves arise from the concurrent progression of chain scission and crosslinking.

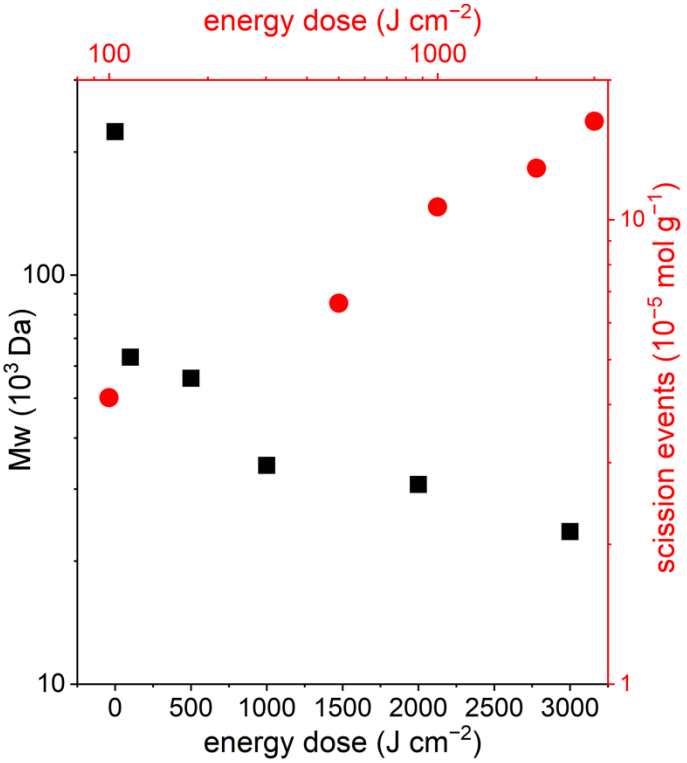

Supplementary Fig. 6 | Molecular weight and scission events of 192-kDa PS vs. energy dosage.

To further elucidate the photodegradation mechanism of the system, IR spectra were recorded for polymer films subjected to different illumination times (Supplementary Fig. 7a). Relative to the as-cast film, the irradiated samples show the gradual appearance of a new absorption band at ~1721 cm^{-1}, which is assigned to carbonyl stretching vibrations and is characteristic of polymer photodegradation. To quantify the extent of degradation, a carbonyl index (CI) was calculated (Supplementary Fig. 7b) as the ratio of the absorbance at the carbonyl band maximum to that of a stable reference band. In this system, the aromatic C=C stretching vibration at 1600 cm^{-1} was used as the internal reference. The CI is therefore expressed as:

$$CI = \frac{A_{abs\,(1721\,cm^{-1})}}{A_{abs\,(1600\,cm^{-1})}} \tag{S4}$$

All absorbance values were subjected to linear baseline correction to account for baseline drift induced by photodegradation; the baseline correction regions are summarized in Supplementary Table 2.

The CI increases with illumination time (Supplementary Fig. 7b), indicating a steady accumulation of carbonyl-containing species and supporting a degradation process dominated by progressive chain scission. Notably, this linear increase closely parallels the linear decrease observed in the contrast curve of the PS/THX (5 wt%) films, providing complementary evidence that photochemical degradation proceeds primarily through backbone cleavage accompanied by formation of polar functional groups, such as carbonyls, which in turn govern the evolution of film solubility.

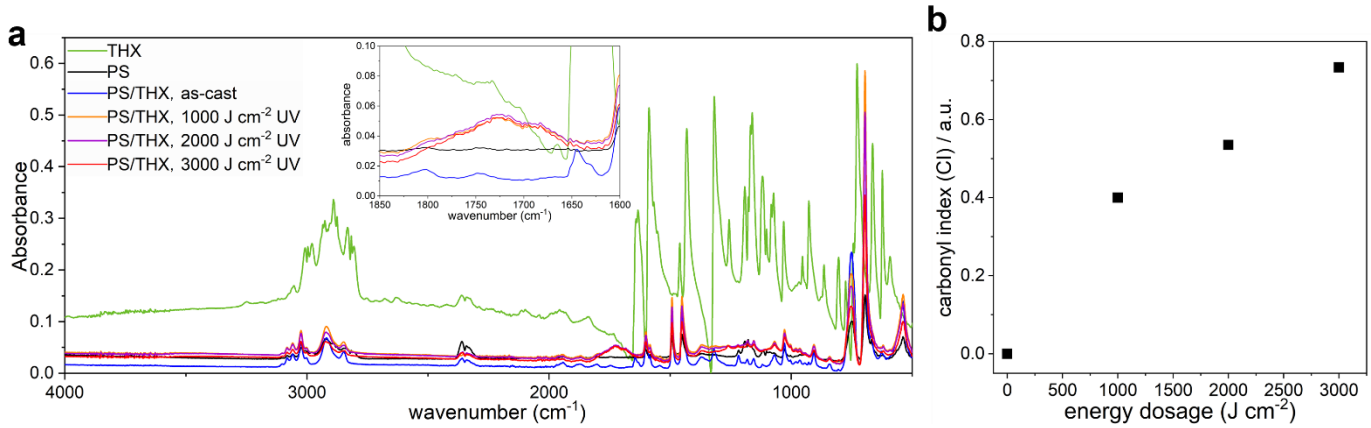

Supplementary Fig. 7 | ATR-FTIR spectra and carbonyl index. a, ATR–FTIR spectra of PS/THX films containing 5wt% THX recorded after different UV exposure dosage and reference samples. **b**, Carbonyl index (CI) extracted from the IR absorbance at 1721 cm^{-1} using the 1600 cm^{-1} band as an internal reference. All the samples were made by 192-kDa PS.

Supplementary Table 2 | Linear Baseline Correction for the PS/THX Samples.

Sample	Absorption band (cm^{-1})	Baseline correction (cm^{-1})
PS/THX	1600	1650–1508
	1721	1840–1630

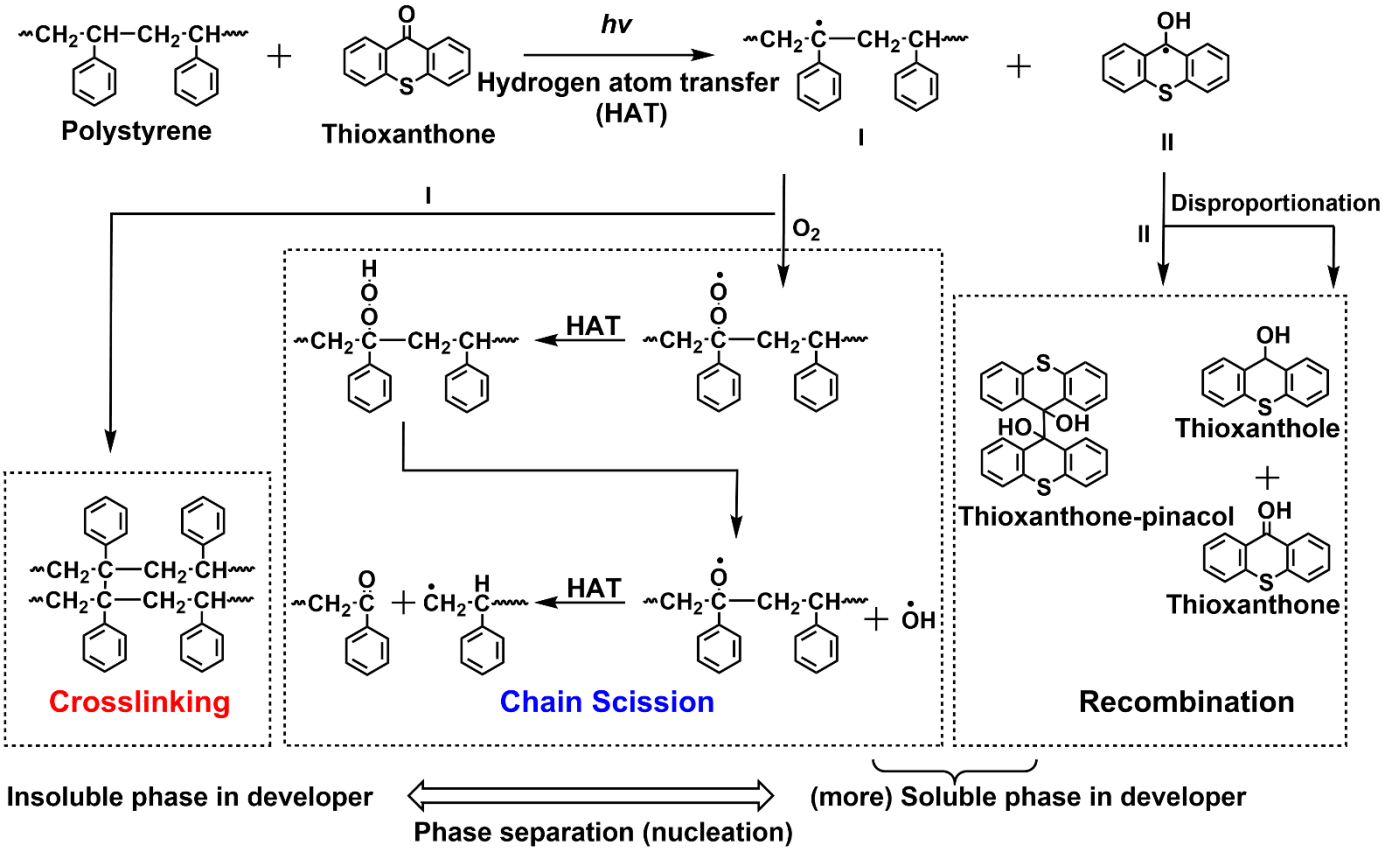

Supplementary Fig. 8 | Schematic illustration of the competing chain scission and crosslinking pathways in the PS/THX under UV irradiation.

To rationalize the observed contrast-curve behaviour together with the complementary GPC, TGA, and ATR-FTIR results discussed above, a photochemical reaction scheme for the PS/THX system is proposed based on the basis of well-established photochemistry of thioxanthone-type sensitizers and related polymer systems reported in the literature (Supplementary Fig. 8)[3–5]. Upon UV irradiation, THX functions as a photosensitizer and is excited to its triplet state, from which it efficiently abstracts a hydrogen atom from the PS backbone via a hydrogen atom transfer (HAT) process. This primary step generates a carbon-centered radical on the PS chain (I) along with a THX ketyl radical (II). The formation of polymer-centered radicals on the PS chain (I) represents a critical branching point in the photochemical response, as these species can follow competing reaction pathways leading to either crosslinking or chain scission.

On the one hand, recombination of adjacent polymer radicals results in the formation of covalent interchain bonds, producing a crosslinked network that is insoluble in the developer. This crosslinked fraction act as a mechanically robust skeleton that remains intact even after prolonged irradiation and development, consistent with the non-zero residual fraction observed in the contrast curves at high exposure doses.

On the other hand, in the presence of oxygen, polymer radicals readily react to form peroxy radicals, which can subsequently undergo hydrogen abstraction or disproportionation reactions. These processes promote β-scission of the PS backbone, yielding lower-molecular-weight fragments and oxygen-containing functionalities, such as carbonyl groups. The accumulation of such chain-scission events progressively enhances the solubility of the material in acetic acid, accounting for the continuous decrease in the remaining fraction with increasing exposure dose observed in the contrast curves.

In parallel, THX-derived radicals may recombine to form thioxanthone pinacol or undergo back-reactions that regenerate thioxanthone or yield thioxanthol. Although these pathways do not directly contribute to network formation, they reflect the dynamic radical processes occurring during irradiation. Overall, the photochemical behaviour of the PS/THX system is governed by a competition between chain scission, which facilitates dissolution during development, and crosslinking, which stabilizes the insoluble phase. This interplay provides a coherent explanation for the concentration-dependent contrast behaviour and underpins the optimal foaming performance observed at intermediate THX loadings.

Supplementary Note 3

Prediction of Bubble Growth Kinetics Exponents

We consider the bubble growth kinetics underlying film expansion by measuring growth exponents of the change in film height Δh as a function of time. All traces in Fig. 3a show up to three regimes with different growth exponents. Note that times t and growth heights $\Delta h(t)$ are normalized by t_b and $\Delta h(t_b)$, the time and height grown when the solvent reaches the base of the film, estimated from early SEM sections of the film growth. The method used to estimate t_b is given below.

The initial stages of film growth are governed by progressive nucleation of bubbles as the developing solvent diffuses deeper inside the film. We model how the height of the film changes by assuming that the film height broadly scales with the total number and growth dynamics of the bubbles in the film as they are nucleated. As stated in the manuscript, we assume that individual bubbles grow by a scaling $\propto X t_g^y$, where t_g is the time elapsed since nucleation, X is a constant which scales with bubble nucleation density, and $y = 1$. This exponent is corroborated directly in Fig. 3b and is consistent with progressive transport of solute into the bubble, keeping the osmotic pressure difference between the inside and outside of the bubbles roughly constant.

Given the above, the growth of the film over time may be approximated as

$$\Delta h(t) \approx \int_0^{z_f} X t_g^y \, dz \tag{S5}$$

where z corresponds to distance from the upper surface of the original film, and z_f is the position down to which the solvent has reached at time t. Assuming case II diffusion, the position of the front migrates as $z_f \propto Kt$, where K is a constant. Thus, t_g for bubbles at a position z may be expressed as $t_g = t - \frac{z}{K}$.

The above integration yields $\Delta h(t) \approx \frac{XK}{2} t^2$. Thus, $\Delta h(t) \propto t^2$ at early times.

After the solvent has permeated the film, we note that the bubbles grow quickly enough to have filled out the majority of the film volume. At this point, the film growth reduces to isotropic swelling due to the continued presence of the solute. Assuming the solute has not left the film for the solvent reservoir yet at this time, the expansion rate is governed by osmotic pressure according to Van't Hoff's law. If there are N_s moles of solute in the film, the osmotic pressure Π is given by $\Pi V = N_s RT$ where V is the volume of the film, R is the molar gas constant, and T is the temperature. The rate of change of film volume is governed by the pressure such that $\frac{dV}{dt} = m\Pi$, where m is the permeability of the top of the film. Thus, we get $\frac{dV}{dt} = \frac{mN_s RT}{V}$. Note that the volume is given by $V = Ah$, where A is lateral cross-section of the film, and h is the height. Since $dV = Adh$, we get $A\frac{dh}{dt} = \frac{mN_s RT}{Ah}$, yielding $h^2 \propto t$ or $h \propto t^{0.5}$.

Supplementary Note 4

Estimation of Time t_b Taken for Solvent to Reach Base

In this work, we present time and growth heights for growing and collapsing foams rescaled by t_b, the time taken for the solvent to reach the base, and $\Delta h(t_b)$, the amount by which the foam height has grown at this time. We assume a linear front velocity (case II diffusion), as evidenced by CLSM and spectrometric measurements (see Supplementary Note 1). We note that the accuracy of t_b does not affect the functional form of the growth curves.

Once t_b is determined, $\Delta h(t_b)$ is found via a linear interpolation between data points.

Fig. 3a, growth curves for 192-kDa polystyrene

(1) 2000 J cm^{-2} exposure, 22°C development

Linear fit to first two points.

Estimate: $t_b = 570$ s

(2) 3000 J cm^{-2} exposure, 32°C development

Linear fit to first three time points.

Estimate: $t_b = 41$ s

(3) 3000 J cm^{-2} exposure, 62°C development

Before first time point $t = 5$ s, take mid-point.

Estimate: $t_b = 2.5$ s

Fig. 4b, collapse curves for 35-kDa polystyrene

(4) 500 J cm^{-2} exposure, 22°C development

Base just reached at first time point $t = 25$ s

Estimate: $t_b = 25$ s

(5) 1000 J cm^{-2} exposure, 22°C development

Linear extrapolation from zero + first point $t = 5$ s.

Estimate: $t_b = 13.8$ s

(6) 2000 J cm^{-2} exposure, 22°C development

Linear extrapolation from zero + first point $t = 5$ s.

Estimate: $t_b = 10.8$ s

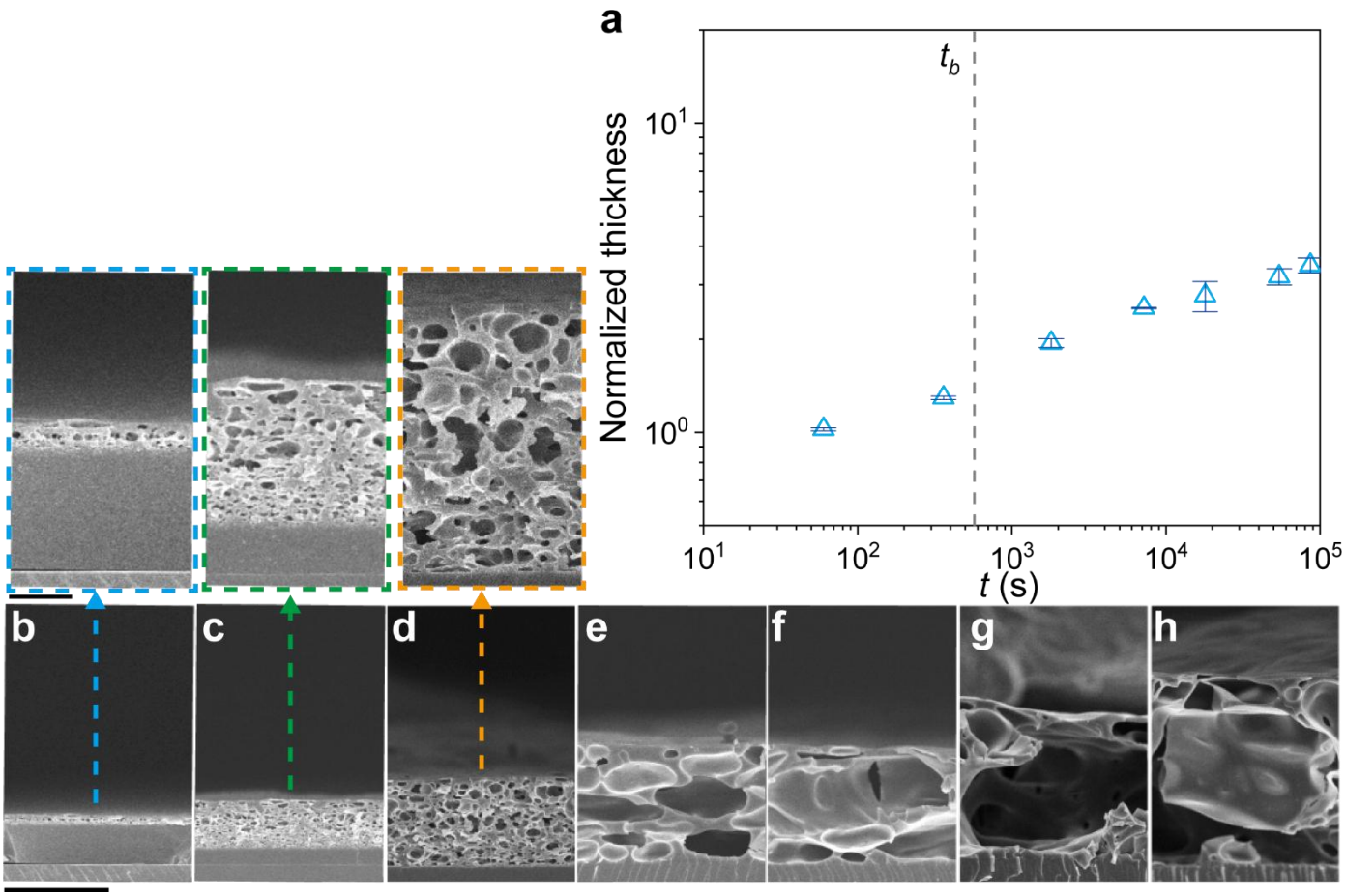

Supplementary Fig. 9 | DFP film growth as a function of time at a lower development temperature. **a**, Normalized DFP film thickness versus development time, normalized by the as-UV-exposed thickness. Error bars denote standard deviation (n = 3). **b**–**h**, SEM cross-section of the DFP film after a development time of 1 min (**b**), 6 min (**c**), 30 min (**d**), 2 hours (**e**), 5 hours (**f**), 15 hours (**g**), and 24 hours (**h**), respectively. Scale bar: 10 μm in the primary panels and 2 μm in the zoom-in panels. 192-kDa polystyrene films with a thickness of 4.7 μm were prepared by spin-casting a solution containing 5 wt% thioxanthone relative to the polymer. UV exposure was performed in a custom LED chamber (Thorlabs, λ_i: 385 nm) with an energy dosage of 2000 J cm^{-2}. The UV-exposed films were developed in acetic acid at 22 ± 1°C. This result corresponds to the blue triangles in Fig. 3a in the main text.

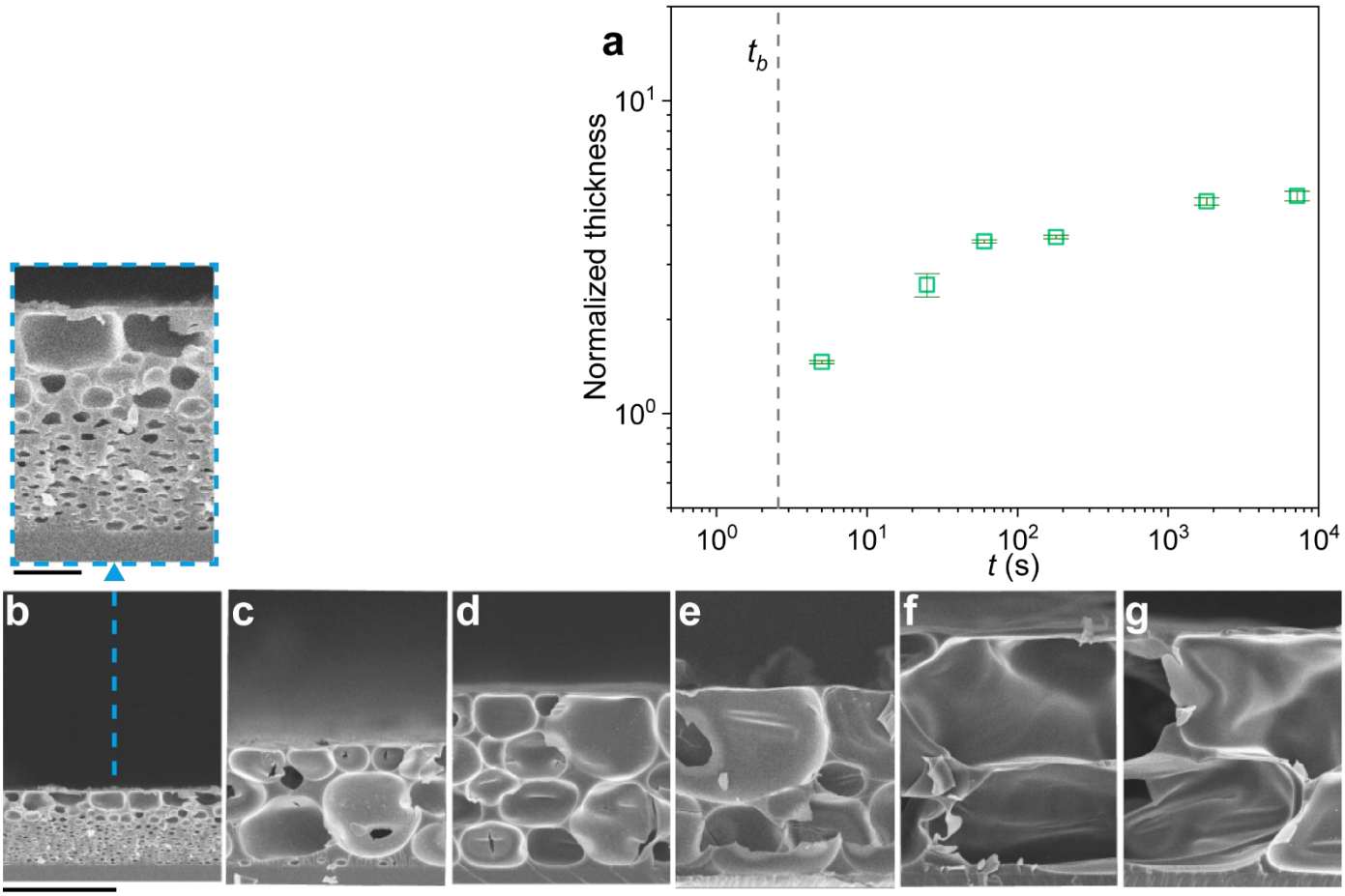

Supplementary Fig. 10 | DFP film growth as a function of time at a higher development temperature. a, Normalized DFP film thickness versus development time, normalized by the as-UV-exposed thickness. Error bars denote standard deviation (n = 3). **b**–**g**, SEM cross-section of the DFP film after a development time of 5 s (**b**), 25 s (**c**), 1 min (**d**), 3 min (**e**), 30 min (**f**), and 2 hours (**g**), respectively. Scale bar: 10 μm in the primary panels and 2 μm in the zoom-in panels. 192-kDa polystyrene films with a thickness of 4.7 μm were prepared by spin-casting a solution containing 5 wt% thioxanthone relative to the polymer. UV exposure was performed in a custom LED chamber (Thorlabs, λ_i: 385 nm) with an energy dosage of 3000 J cm^{-2}. The UV-exposed films were developed in acetic acid at 62 ± 1°C. This result corresponds to the green squares in Fig. 3a in the main text.

Supplementary Note 5

Light Transport Mean Free Path (l_t)

Method

The light scattering capability of DFP samples can be characterized by a transport mean free path (l_t). A shorter l_t implies faster randomization of the propagation paths of light entering the medium, hence stronger scattering strength.

First, the total transmittance spectrum (T_{tot}) of developed samples was measured by a UV-vis-NIR spectrophotometer (Hitachi 4100) equipped with an integrating accessory (Φ60 full-sphere, P/N 1J1-0100). The T_{tot} spectra exhibit an initial decrease followed by a subsequent increase over the broadband spectral range as a function of development time (see Fig. 3c in the main text, as also reshown on the right). We also require the original and foamed thickness of the film, h_0 and h_f, as determined from 2D SEM cross-sections. l_t of films with development time (t) greater than t_b may then be calculated based on the diffusion theory (Supplementary Fig 11a). The relationship between the T_{tot} and the foamed thickness h_f, as well as its subsequent rearrangement giving l_t, are defined in Equation S6[6]:

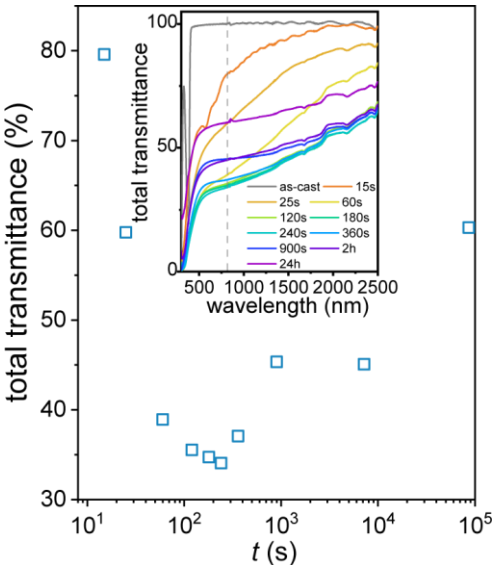

Fig 3c in the main text. Total transmittance at 810 nm (primary panel) and VIS-IR (inset) over development time. The samples were prepared under standard conditions.

$$l_t = \frac{T_{tot} h_f}{1 + z_e - 2 z_e T_{tot}} \tag{S6}$$

where z_e is a phenomenological parameter to account for the behaviour of photons near boundaries under the diffusion approximation, making the diffuse photon concentration field $U(\vec{r})$ extrapolate to zero at a distance $z_e l_t$ outside the sample. z_e can be taken as:

$$z_e = \frac{2}{3} \frac{1 + \int_0^1 3\varphi^2 R(\varphi) d\varphi}{1 + \int_0^1 2\varphi R(\varphi) d\varphi} \tag{S7}$$

where $R(\varphi)$ is the total reflection probability on the boundary between interior scattering media and exterior environment with an incident angle $\theta_i = \cos^{-1}\varphi$. When θ_i exceeds the critical angle for total internal reflection, $R(\varphi)$ equals unity. Conversely, when θ_i is below this critical angle, $R(\varphi)$ corresponds to the Fresnel reflectance at the interface. Both p and s polarization reflectance should be included.

$$R(\varphi) = 0.5R(\varphi)_p + 0.5R(\varphi)_s \tag{S8}$$

$$R(\varphi)_p = \left(\frac{n_i \cos(\theta_e) - n_e \cos(\theta_i)}{n_i \cos(\theta_e) + n_e \cos(\theta_i)}\right)^2 \tag{S9}$$

$$R(\varphi)_s = \left(\frac{n_i \cos(\theta_i) - n_e \cos(\theta_e)}{n_i \cos(\theta_i) - n_e \cos(\theta_e)}\right)^2 \tag{S10}$$

where n_i and n_e are the interior and exterior indices, respectively. θ_e is the emergence angle following the Snell's law. Considering that the DFP film is much thinner than the thickness of glass substrate, the exterior index is given by the refractive index of glass (n_e = 1.52) while the interior index is the effective index n_{eff} of the DFP structure:

$$n_{\text{eff}} = \sqrt{\frac{1+2\alpha}{1-\alpha}}, \alpha = \frac{(1-f)(n_{PS}{}^2-1)}{n_{PS}{}^2+2} \quad \text{(S11)}$$

where f is the filling fraction of air in the structures (*i.e.*, porosity) and n_{PS} is the refractive index of polystyrene, respectively. The filling fraction of air is calculated by

$$f = 1 - \frac{h_0}{h_f}, \; t > t_b \quad \text{(S12)}$$

where h_0 and h_f are the thickness of film before and after development, respectively. Supplementary Fig 11b shows the thickness of foaming area and filling fraction of air. Supplementary Fig 11c shows the calculated z_e and l_t.

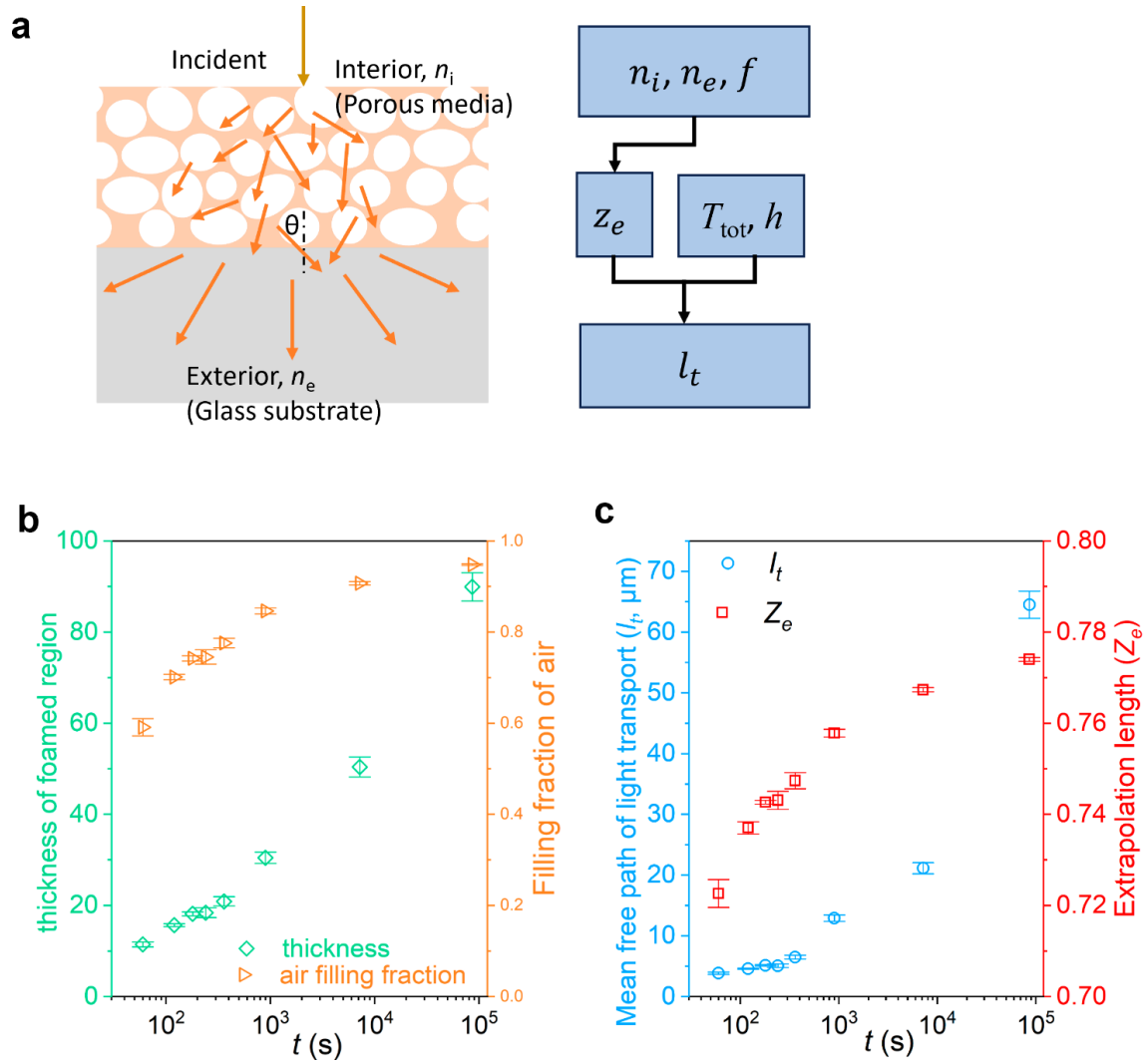

Supplementary Fig. 11 | Mean free path of light transport (l_t). a, Calculation model for z_e and l_t. **b**, Thickness of foamed region and filling fraction of air as a function of development time. Error bars denote standard deviation (n = 3). **c**, Calculated z_e and l_t as a function of development time. Error bars denote standard deviation (n = 3). The polystyrene/thioxanthone films are prepared in standard conditions: 4.7-μm-thick polystyrene films were spin-cast on cover glass using a polymer solution containing 5 wt% thioxanthone (photoinitiator) relative to polymer. The films were illuminated using a custom LED chamber (Thorlabs, λ_i: 385 nm) for 3000 J cm^{-2} and then developed in 32℃ acetic acid for different times.

Supplementary Note 6

References for Fig. 3d in the Main Text

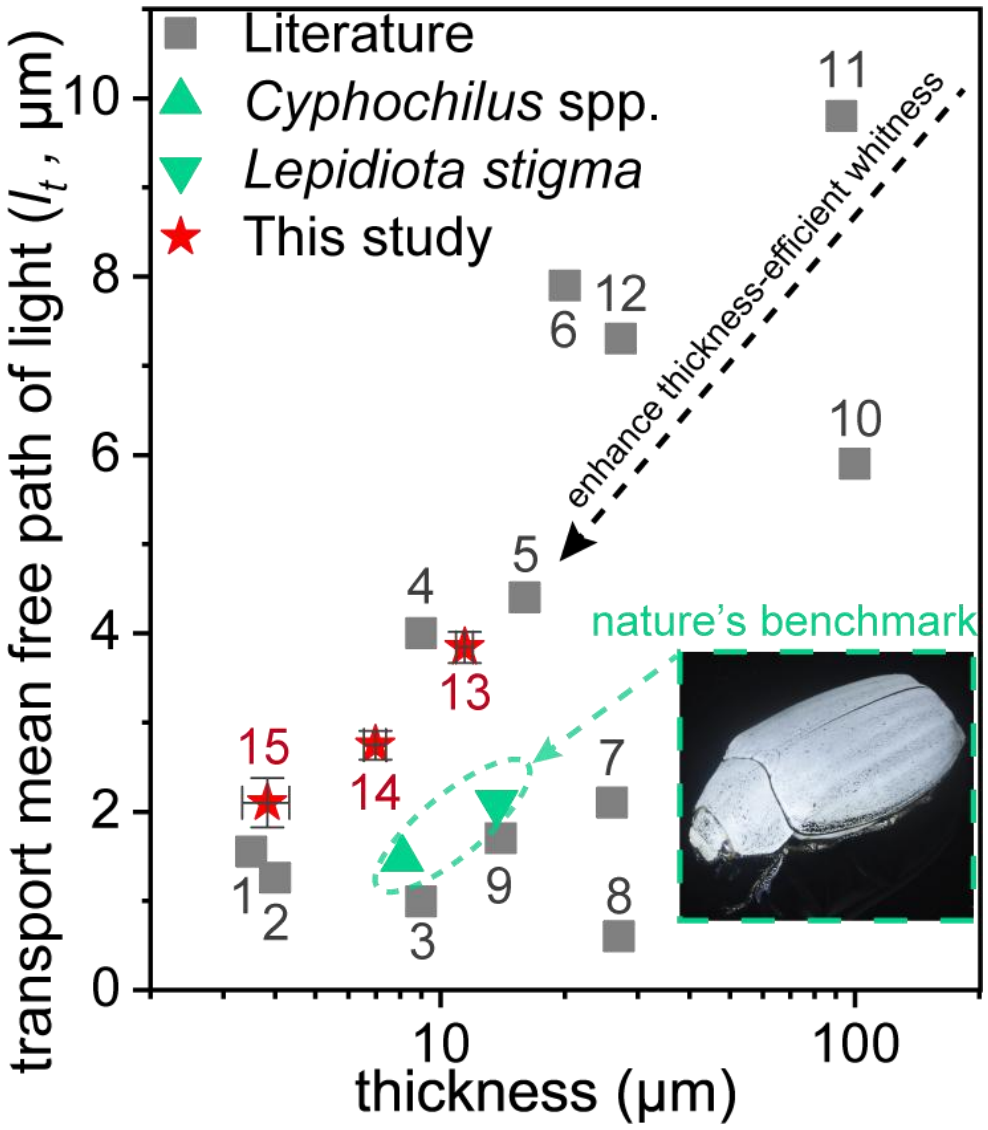

5

Number in the Figure	Material	Thickness (μm)	Transport mean free path of light (μm)	Reference
	Cyphochilus spp.	8.1	1.47	Burresi, M. et al. Bright-White Beetle Scales Optimise Multiple Scattering of Light. *Sci. Rep.* **4**, 6075 (2014).
	Lepidiota stigma	13.7	2.1	
1	polystyrene	3.5	1.55	Zou, W. et al. Biomimetic Polymer Film with Brilliant Brightness Using a One-Step Water Vapor–Induced Phase Separation Method. *Adv. Funct. Mater*. **29**, 1808885 (2019).
2	PMMA	4	1.26	Syurik, J., Jacucci, G., Onelli, O. D., Hölscher, H. & Vignolini, S. Bio-inspired Highly Scattering Networks via Polymer Phase Separation. *Adv. Funct. Mater.* **28**, 1706901 (2018).

3	cellulose particles	9	0.99	Yang, H., Jacucci, G., Schertel, L. & Vignolini, S. Cellulose-Based Scattering Enhancers for Light Management Applications. *ACS Nano* **16**, 7373–7379 (2022).
4	PMMA	9	4	Syurik, J. et al. Bio-inspired, large scale, highly-scattering films for nanoparticle-alternative white surfaces. *Sci. Rep.* **7**, 46637 (2017).
5	poly(BMA-co-EDMA)	16	4.4	Tang, Y. *et al.* Bioinspired high-scattering polymer films fabricated by polymerization-induced phase separation. *Opt. Lett.* **45**, 2918-2921 (2020).
6	SiO_2 microspheres	20	7.9	Effective Radiative Cooling by Paint-Format Microsphere-Based Photonic Random Media. *ACS Photonics* **5**, 1181–1187 (2018).
7	porous nano silk	26	2.1	Park, B. K., Han, S. M. & Han, S. E. Surpassing Cyphochilus scales in optical scattering strength by well-controlled electrospun nanostructures. *Opt. Mater. Express* **12**, 2529-2540, (2022).
8	ZnO nanoparticle	27	0.6	Kim, M. et al. Maximal energy transport through disordered media with the implementation of transmission eigenchannels. *Nat. Photonics* **6**, 581–585 (2012).
9	porous fluoropolymer	14	1.7	Yu, B. et al. Biomimetic Porous Fluoropolymer Films with Brilliant Whiteness by Using Polymerization-Induced Phase Separation. *Adv. Mater. Interfaces* **9**, 2101485 (2022).
10	cellulose	100	5.9	Caixeiro, S., Peruzzo, M., Onelli, O. D., Vignolini, S. & Sapienza, R. Disordered Cellulose-Based Nanostructures for Enhanced Light Scattering. *ACS Appl. Mater. Interfaces* **9**, 7885–7890 (2017).
11	polystyrene	93	9.8	Mandal, J. et al. Hierarchically porous polymer coatings for highly efficient passive daytime radiative cooling. *Science* **362**, 315-319 (2018).
12	TPU	27.3	7.3	Liu, X. et al. Biomimetic Photonic Multiform Composite for High-Performance Radiative Cooling. *Adv. Opt. Mater*. **9**, 2101151 (2021).
13	polystyrene	11.4±0.5	3.8±0.2	**This study**. 192-kDa polystyrene. As-cast thickness is 4.7±0.2 μm. T_{tot} at 810 nm is 38.9%. Error bar denotes standard deviation (n = 3).
14	polystyrene	7.0±0.4	2.7±0.2	**This study**. 192-kDa polystyrene. As-cast thickness is 3.1±0.1 μm. T_{tot} at 810 nm is 43.2%. Error bar denotes standard deviation (n = 3).
15	polystyrene	3.8±0.5	2.1±0.3	**This study**. 192-kDa polystyrene. As-cast thickness is 2.0±0.1 μm. T_{tot} at 810 nm is 52.7%. Error bar denotes standard deviation (n = 3).

Note: PS denotes polystyrene. PMMA denotes poly(methyl methacrylate), poly(BMA-co-EDMA) denotes poly(butyl methacrylate-co-ethylene dimethacrylate), and TPU denotes thermoplastic polyurethane.

Supplementary Note 7

Evaluation of Porosity via Multiple Techniques

Method

Mechanical properties of the DFP films were analysed by nanoindentation (Elionix ENT2100) at an applied force of 100 μN. The experiments were conducted for both 192-kDa and 35-kDa polystyrene (PS), with the experimental conditions kept the same as in the plots (red circles) shown in Fig. 3a and Fig. 3f in the main text, respectively. Briefly, the thioxanthone (THX) to polymer ratio was kept at 5 wt% for both 192-kDa and 35-kDa PS. UV exposure was conducted using a custom LED chamber (Thorlabs, λ_i: 385 nm). The energy dosage and development temperature for 192-kDa PS films are 3000 J cm^{-2} and 32℃, respectively. The energy dosage and development temperature for 35-kDa PS are 1000 J cm^{-2} and 22℃, respectively. The Young's modulus was measured for PS films developed for different times. These measurements were used to evaluate the porosity of the DFP films according to the Gibson-Ashby Model using Equation S13.

$$\Phi_m = \left(1 - \sqrt{\frac{E}{E_0}}\right) \times 100\% \tag{S13}$$

where Φ_m is the porosity evaluated from the Young's modulus, E and E_0 are the Young's modulus of the foamed and the as-illuminated film, respectively.

The porosity evaluation was checked with two independent experimental approaches: film thickness change measured from the SEM cross-sections, and the analysis of 3D structural models from FIB-SEM characterization. Equation S14 and S15 are used for calculating porosity based on film thickness changes.

$$\Phi_h = \left(\frac{h-h_0}{h}\right) \times 100\%, \quad t \geq t_b \tag{S14}$$

$$\Phi_h = \left(\frac{h-h_0}{h_{porous}}\right) \times 100\%, \quad t < t_b \tag{S15}$$

where Φ_h is the porosity evaluated from thickness expansion, h is thickness of the developed film and h_0 is thickness of as-illuminated film. Equation S14 is used to estimate the porosity when development time is equal to or greater than t_b (the time when solvent diffusion front touched the base of film). Equation S15 is used to estimate the porosity when development time is smaller than t_b, where h_{porous} is the thickness of the porous layer. Here, h, h_0, and h_{porous} are all obtained from cross-sectional SEM images.

Equation S16 is used for the calculation of porosity based on FIB-SEM characterization.

$$\Phi_{FIB} = \left(\frac{\sum V_{pore}}{V_{total}}\right) \times 100\% \tag{S16}$$

where $\sum V_{pore}$ is the volume of all the pores in the 3D spatial model, and V_{total} is the total volume of the 3D spatial model, respectively.

Results and discussion

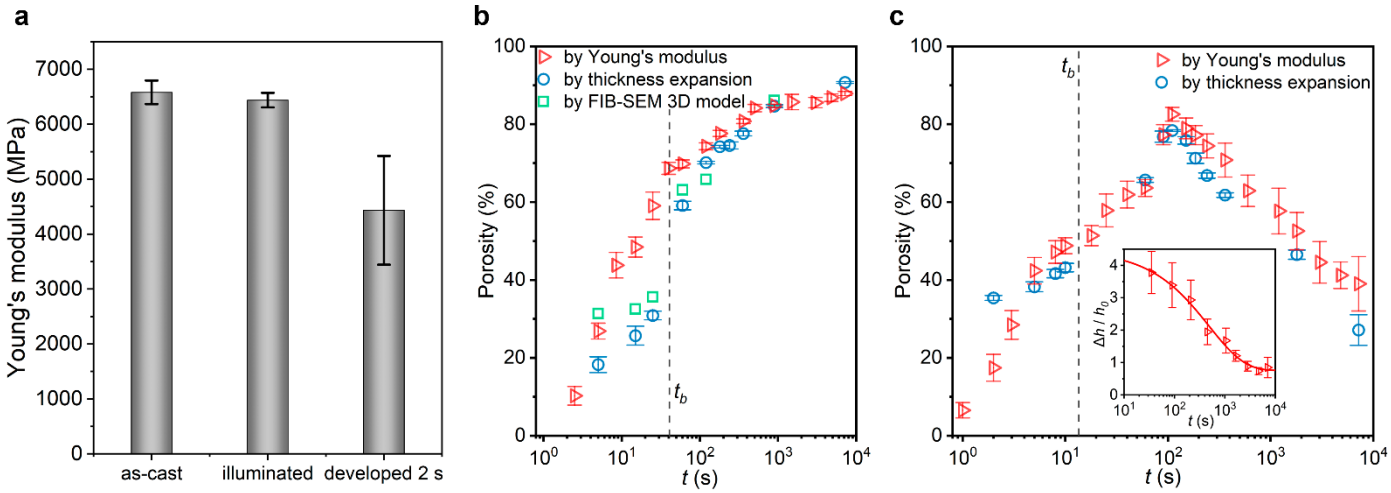

Supplementary Fig. 12 | Mechanical properties and porosity evaluation based on Young's modulus, film thickness change, and FIB-SEM characterization. a, Young's Modulus of as-cast, as-illuminated, and developed 35-kDa PS film. Development time is 2 s. Error bars denote standard deviation (n = 7). **b**, Porosity evaluation for the 192-kDa PS/THX films developed in acetic acid with different times (energy dosage: 3000 J cm^{-2}, development temperature: 32°C). The porosity values from film thickness change and that from 3D structural models by FIB-SEM were included for the comparison. **c**, Porosity evaluation for the 35-kDa PS/THX films developed in acetic acid with different times (energy dosage: 1000 J cm^{-2}, development temperature: 22°C). Inset is $\Delta h/h_0$ derived from Young's modulus vs. time since the initiation of collapse. The porosity values from film thickness change based on SEM observation were included for the comparison. In (**b**) and (**c**), error bars denote standard error of the mean (n = 7 for the data from Young's modulus; n = 3 for the data from film thickness change).

Preliminary characterisation was carried out on the as-cast and illuminated films, prior to development. Within error, there was no notable difference in measured film mechanical properties (via nanoindentation) before and after exposure for the longest exposures for each molecular weight studied (Supplementary Fig. 12a). Whereas one might expect the increase in scission products to soften the pre-swelled polymer film, there is sufficient cross-linked polymer to mask the difference in mechanical property. We note that TGA revealed both a loss of scission products at approximately 350 °C, with mass loss increasing with irradiation time, and an increase in crosslinked PS, as signified by a persistent tail at temperatures where un-crosslinked PS would be thermally degraded.

Mechanical strength measurements of the DFP films were also studied to understand the foam dynamics. Porosity, a key feature of the foamed film, was evaluated using the Young's modulus based on the Gibson-Ashby Model[7]. Supplementary Fig. 12b shows that the porosity increases with time for the 192-kDa polystyrene film. The data is consistent with what is seen for film height (Δh) as a function of time (the red-circle plot in Fig. 3a in the main text): porosity scales with different exponents in three different regimes: (1) a case-II diffusion dominated regime as solvent front not reaching the base of film yet, followed by (2) a pore growth regime driven by hypotonic permeation of the solvent, and (3) a retardation of porosity growth to a plateau in the coarsening stage.

The porosity evaluated by Young's modulus is consistent with porosity estimated from film thickness expansion measured from SEM cross-sections and 3D spatial models from FIB-SEM characterization. The three datasets agree in general, especially for the data after solvent reaching the base of the film ($t \geq t_b$). There is some discrepancy between the porosity by Young's modulus and the other two datasets in the regime of $t < t_b$. This can be explained as the form of the Gibson-Ashby model used here assumes a dominant contribution from the edges of a foam structure. At early times, the pores are still spaced out, with no doubt a significant elastic response from the faces of each cell as well as the unfoamed polymer situated between pores.

Porosity analysis based on Young's modulus was also conducted for the 35-kDa PS film and compared with those evaluated from film thickness change (Supplementary Fig 12c). The data indicates the same trend with the change of film height (Δh) as a function of time (the red-circle plot in Fig. 3f in the main text): porosity changes with different exponents in three different regimes: (1) a case II diffusion dominated regime ($t < t_b$), followed by (2) a pore growth and coarsening regime to reach the maximum, and (3) a reduction regime as the film turns to collapse. The maximum of porosity shows up exactly at the same time with the greatest thickness expansion observed by SEM cross-section. The result indicates that porosity maximum can be used as indicator as the onset in the collapse analysis.

Cross-validation of porosity evaluation was also conducted by again comparing with porosity estimated from film thickness expansion as taken from SEM cross-sections. The two datasets agree well in general, reinforcing the credibility of the findings. A more obvious discrepancy between the two datasets lies in the very short development time (t = 2 s), no doubt caused by the same incomplete foam formation as seen for in 192 kDa polystyrene foam.

While DFP domains strongly resemble liquid foams, many of the driving forces governing rupture and retraction clearly do not apply. For example, there is no drainage along foam borders, and no generation of droplets on film rupture[8]. Thus, we consider a viscoelastic relaxation of the foam; film rupture releases elastic energy which allows the structure to relax. This is consistent with the combination of plasticity (mobile short-chain segments) and elasticity (cross-linking) seen in the film. Also, if the top of the film ruptures, there is nothing to prevent short-chain segments from escaping the film quickly. Thus, the hypotonic pressure suddenly disappears, leaving a further force imbalance which will lead to film relaxation. We analyse the change in film height with time since the initiation of collapse; due to their availability and consistency with measurements from SEM cross-sections, we derive heights from nanoindentation measurements. As shown in the inset of Supplementary Fig. 12c, the height relaxation is fit well by a Kohlrausch-Williams-Watt (KWW) stretched exponential[9]. This is known to correspond to dynamical heterogeneity in arrested systems, consistent with viscoelastic response in a cross-linked polymer network[10]. Fitting to $h(t) \propto e^{-\left(\frac{t}{t_0}\right)^a}$, we find that $a = 0.62 \pm 0.45$ and $t_0 \approx 500$ s in the inset of Supplementary Fig. 12c; $a < 1$ suggests a distribution of relaxation times. In the case of DFP, this is likely to correspond to the simultaneous relaxation of the cross-linked network component and the polymer which surrounds it.

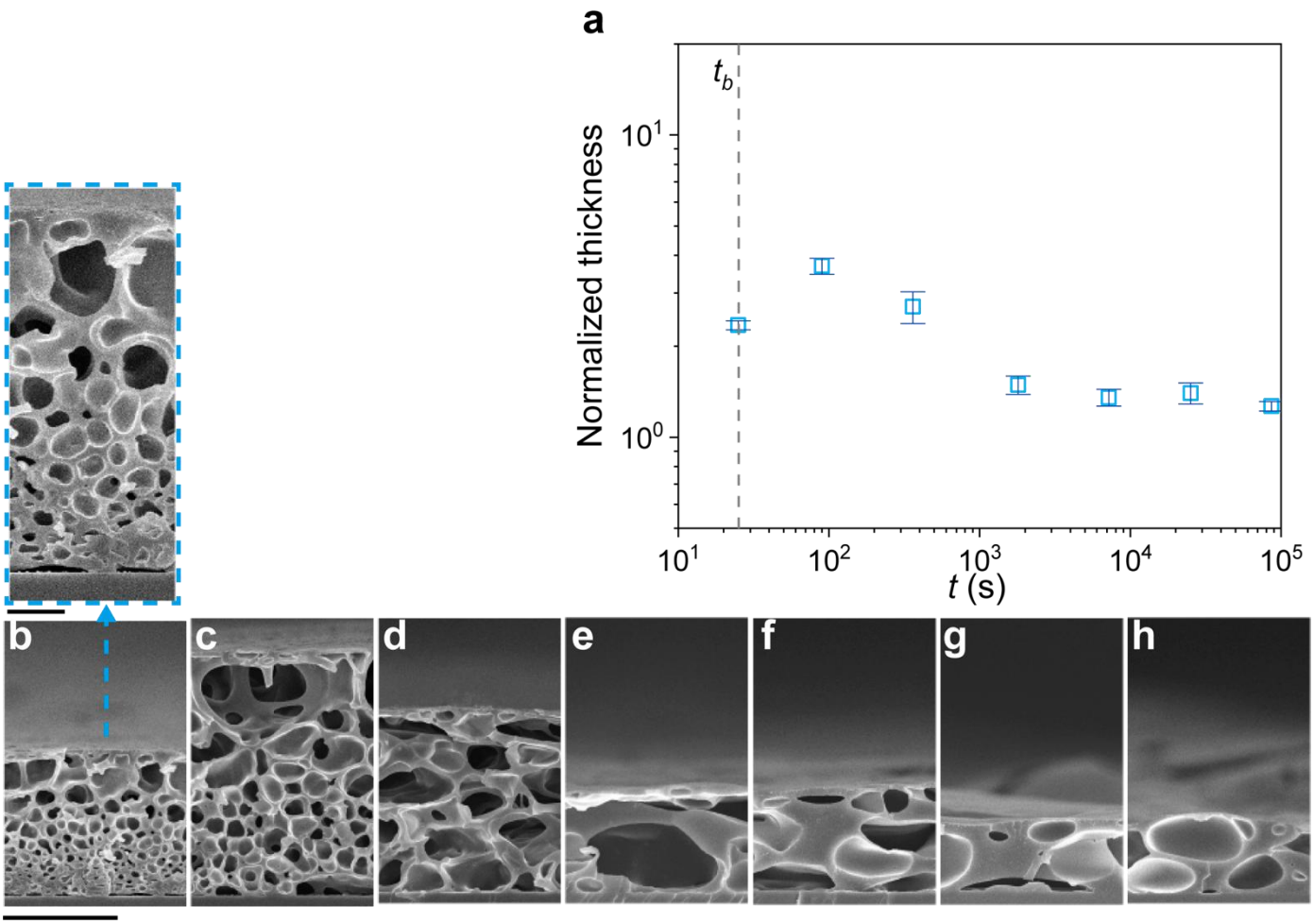

Supplementary Fig. 13 | Structural evolution of 35-kDa polystyrene DFP film under a lower energy dosage. **a**, Normalized DFP film thickness versus development time, normalized by the as-UV-exposed thickness. Error bars denote standard deviation (n = 3). **b**–**h**, SEM cross-section of the DFP film after a development time of 25 s (**b**), 1.5 min (**c**), 6 min (**d**), 30 min (**e**), 2 hours (**f**), 7 hours (**g**), and 24 hours (**h**), respectively. Scale bar: 5 μm in the primary panels and 1 μm in the zoom-in panels. 35-kDa polystyrene films with a thickness of 2.7 μm were prepared by spin-casting a solution containing 5 wt% thioxanthone relative to the polymer. UV exposure was performed in a custom LED chamber (Thorlabs, λ_i: 385 nm) with an energy dosage of 500 J cm^{-2}. The UV-exposed films were developed in acetic acid at 22 ± 1°C. This result corresponds to the blue squares in Fig. 3f in the main text.

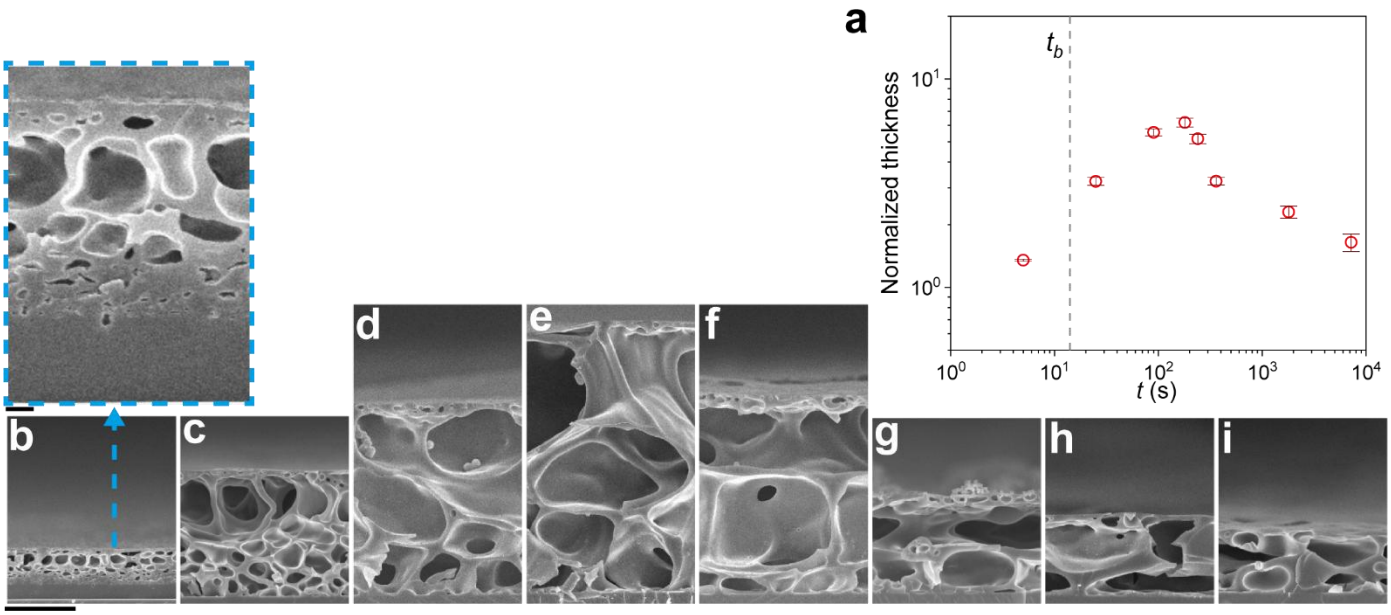

Supplementary Fig. 14 | Structural evolution of 35-kDa polystyrene DFP film. a, Normalized DFP film thickness versus development time, normalized by the as-UV-exposed thickness. Error bars denote standard deviation (n = 3). **b**–**i**, SEM cross-section of the DFP film after a development time of 5 s (**b**), 25 s (**c**), 1.5 min (**d**), 3 min (**e**), 4 min (**f**), 6 min (**g**), 30 min (**h**), and 2 hours (**i**), respectively. Scale bar: 5 μm in the primary panels and 2 μm in the zoom-in panels. 35-kDa polystyrene films with a thickness of 2.7 μm were prepared by spin-casting a solution containing 5 wt% thioxanthone relative to the polymer. UV exposure was performed in a custom LED chamber (Thorlabs λ_i: 385 nm) with an energy dosage of 1000 J cm^{-2}. The UV-exposed films were developed in acetic acid at 22 ± 1°C. This result corresponds to the red circles in Fig. 3f in the main text.

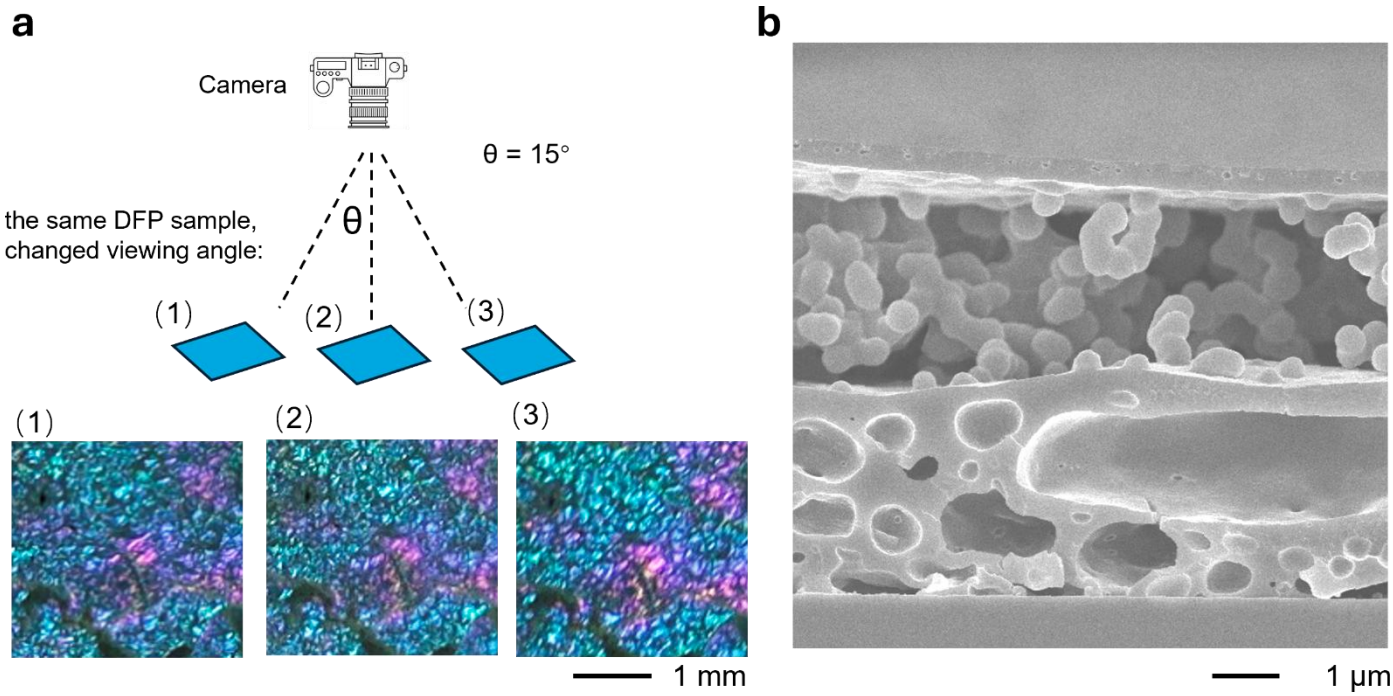

Supplementary Fig. 15 | Structural colours observed in the collapsed DFP films containing microspheres. a, Structural colours of a collapsed 35-kDa polystyrene (PS) film observed with different viewing angles. **b**, SEM cross-sectional image of the collapsed 35-kDa PS DFP film. Scale bars, 1 mm (**a**); 1 μm (**b**). 2.7-μm-thick PS (35 kDa) film with 5 wt% thioxanthone content relative to PS was cast on a cover glass, illuminated using a custom LED chamber (Thorlabs, λ_i: 385 nm) with an energy dose of 2000 J cm^{-2}, and developed in 22°C acetic acid for 25 s. Structural colours related to microsphere formation show colour consistent with a certain range of viewing angle (±15°). However, it is worth noting that such structures are transient and appear to be washed out over longer development times. Elucidation of the formation mechanism for this particular morphology, and how it relates to its apparent iridescence, is left for future work.

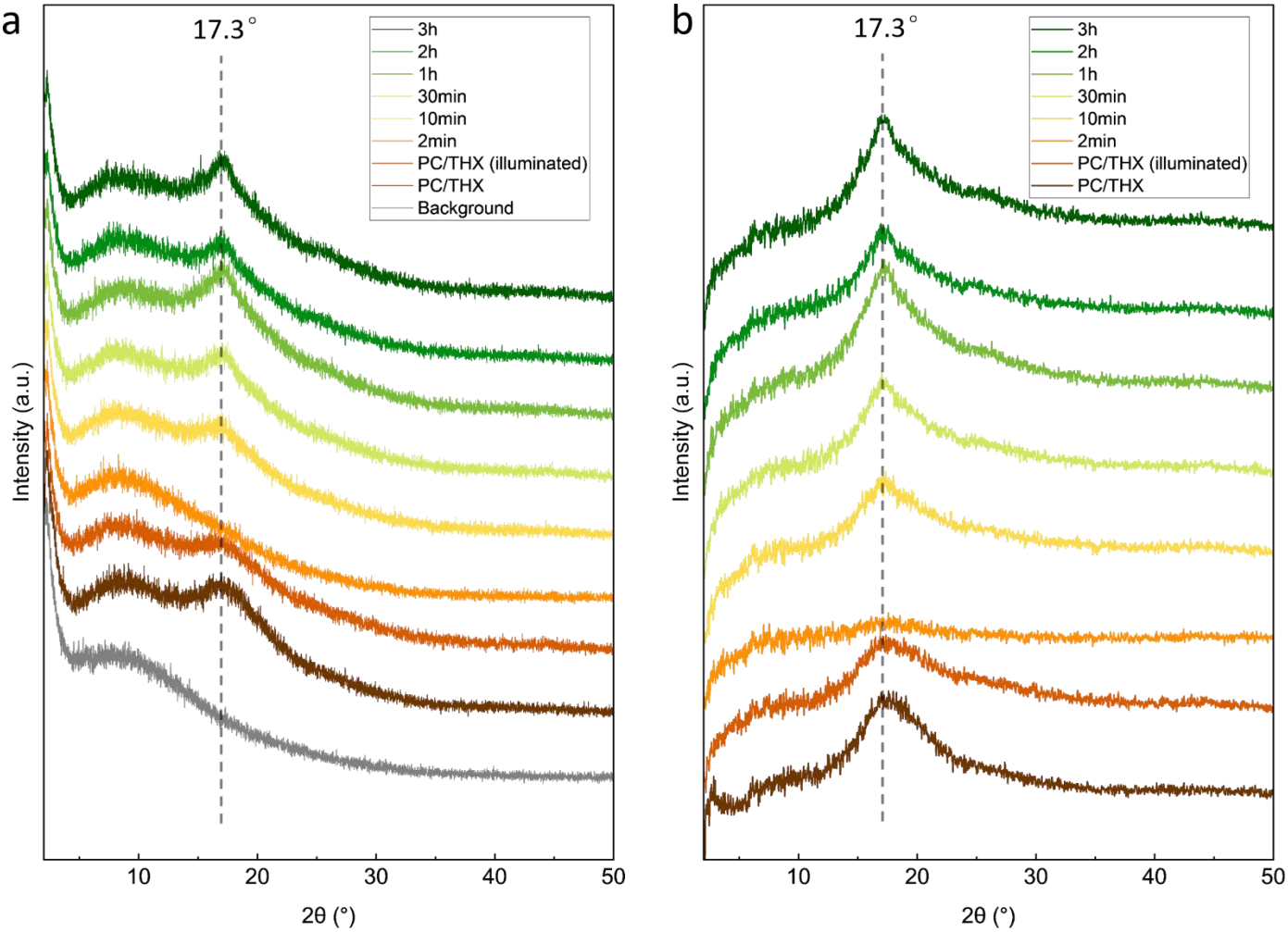

Supplementary Fig. 16 | X-ray Diffraction (XRD) patterns of polycarbonate DPF films with different development times. a, Measured XRD patterns. b, XRD patterns after instrumental background correction. Powder X-ray diffraction (Rigaku MiniFlex 600-C/AC) patterns of the polycarbonate (PC) films were measured using Cu Kα radiation (λ=1.5418 Å) at 15 mA and 40 kV. Data were recorded over a 2θ range of 2–50° with a step of 0.0025° and a scan rate of 4° min^{-1}. 5-µm-thick PC films were prepared by spin-casting using a solution with thioxanthone (THX) to polymer ratio of 7 wt%. The films were irradiated using a broadband UV light source (Metal halide lamp M06-L31, Eye Cure, EYE GRAPHICS Co., Ltd., Japan) with an energy dose of 2000 J cm^{-2}. A 1-mm-thick soda lime glass sheet (AS ONE Co., Ltd., Japan) was used to filter out ultraviolet light below approximately 300 nm. Afterwards, the films were developed in acetic acid at 53 °C for durations ranging from 2 min to 3 h. The developed films were scraped from the cover glass substrates and collected for XRD measurements. XRD patterns were corrected for the non-zero background arising from the sample holder. The characteristic peak at 2θ = 17.3° corresponds to the crystalline region of polycarbonate[11,12]. The sharpening of this diffraction peak with prolonged development duration indicates an increased degree of crystallinity, which, together with SEM-observed growth of microflower structures (Extended Data Fig. 7), shows that the structural evolution of polycarbonate in the collapse phase is associated with a recrystallization process.

Supplementary Note 8

Roughness Measurement by Atomic Force Microscopy (AFM)

Method

The surface roughness of DFP films was characterized by atomic force microscopy (AFM). A 90 μm × 90 μm area (maximum lateral scan area) was scanned in tapping mode by AFM (Asylum Research MFP-3D) using an ACT-200 silicon cantilever to acquire the average roughness (R_a) and root-mean-square roughness (R_q). Mean and standard deviation of R_a and R_q were reported based on the scanning of three samples. The polystyrene (PS, 35 kDa) and polycarbonate (PC) DFP films are prepared in the same conditions as those tested for the water contact angles (Fig. 4g in the main text). 2.7-μm-thick PS (35-kDa) film and 4.2-μm-thick PC film were spin cast on a cover glass with thioxanthone to polymer ratio kept as 7 wt% for both polymers. The films were illuminated in the LED chamber (Thorlabs, λ_i: 385 nm). The energy dose and development temperature for 35-kDa PS films were 1000 J cm^{-2} and 22℃, respectively. The energy dose and development temperature for PC films were 3000 J cm^{-2} and 32℃, respectively. The films were developed over different times to study its effect on surface morphology.

Results and discussion

Surface morphology of DFP films was investigated to elucidate its influence on surface wetting properties. Here, PC and 35-kDa PS films were prepared, and both polymer systems undergo collapse at comparable amounts of development time. Supplementary Figs. 17a and 17b present the AFM and SEM images of the PC films over development time. Supplementary Figs. 17c and 17d present the AFM and SEM images of the PS films over development time. As shown in Supplementary Figs. 17e and 17f, R_a and R_q increases as development time increases from 0 s to 3600 s for both PC and PS films. The R_a and R_q of PC films are about 150 nm higher than those of PS films at the same development time.

Although collapse can make surface rougher for both PS and PC films, only the collapsed PC film is able to achieve superhydrophobicity (see contact angle data in Fig. 4g in the main text). AFM and SEM images of PC films show the formation of microparticles with a diameter of ≈5 μm. Moreover, high-magnification SEM images (see Fig 4c and Extended Data Fig7b in the main text) show the micro/nano hierarchical roughness of the PC microflowers. In contrast, high-magnification SEM image (see Extended Data Fig7c in the main text) indicates such hierarchical roughness is absent in PS films. Our study demonstrates that the micro/nano hierarchical structure plays an important role in achieving superhydrophobicity. This result agrees well with prior studies of superhydrophobic natural surfaces[13].

In addition, it is worth noting that the needle-like nanostructures are hard to see in the AFM images. This is because the relatively large surface undulations from the 5-μm-size microflowers makes the AFM difficult to precisely capture the structural features at the nanometer scale, even when a low scanning rate (0.1 Hz) was adopted for scanning the area of 90 μm × 90 μm (maximum lateral scan area by the instrument).

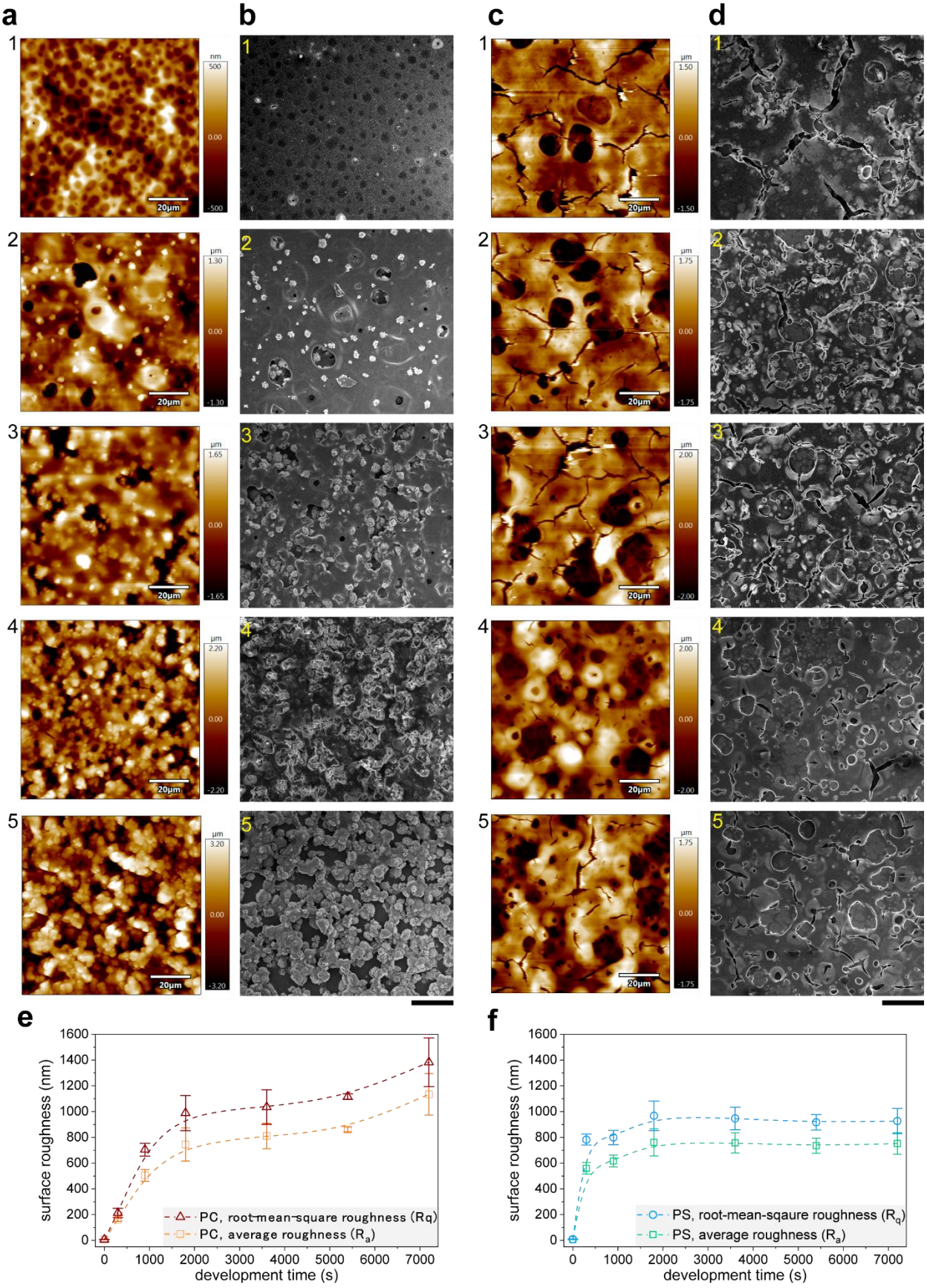

Supplementary Fig. 17 | Surface roughness measured by atomic force microscopy (AFM). **a**, **b**, AFM (**a**) and SEM (**b**) images of polycarbonate (PC) DFP films after different development times. **c**, **d**, AFM (**c**) and SEM (**d**) images of polystyrene (PS, 35kDa) DFP films after different development times. Panel number in (**a**)–(**d**) denote different development times: 6 min (1), 15 min (2), 30 min (3), 1.5 hours (4), and 2 hours (5). **e**, Average roughness (R_a) and root-mean-square roughness (R_q) of PC DFP films vs. development time. **f**, R_a and R_q of PS DFP films vs. development time. In (e) and (f), error bar denotes standard deviation (n = 3). Lines are drawn as a guide to the eye. Scale bars, (**a**)–(**d**) 20 μm.

Supplementary Note 9

Commentary on printing resolution limits and angle-dependent diffractive color

Method

The resolution limit of DFP printing was studied primarily using 192-kDa polystyrene (PS) and thioxanthone (THX). 2.5-μm-thick PS films were prepared by spin-casting a solution in which thioxanthone (THX) was added at 9 wt% relative to the polymer. Unless stated otherwise, cover glass (Product code: 24241, Muto Pure Chemicals Co., Ltd.) is the substrate for casting the films. The film was illuminated either using a maskless micro-LED system or using a custom LED chamber (Thorlabs λ_i: 405 nm) with a chromium photomask. Energy dosage is 200–800 J cm^{-2}. The illuminated films were developed in acetic acid at 32 ℃.

Ultra-high-resolution printing can be performed using a micro-LED illumination instrument (λ_i: 405 nm, Maskless Lithography Tool D-light DL-1000GS/KCH, Nano System Solutions). The micro-LED enables pixel-level control of illumination with a spatial resolution of 1 μm. The D-light DL1000 is integrated with a digital micromirror device (Texas Instruments) to regulate the projected pattern. This electromechanical system comprises 1,024 × 768 micromirrors that can be switched on or off independently. Through a lens, these mirrors direct light onto 1 μm × 1 μm regions, yielding an exposure field of 1,024 μm × 768 μm per frame. Larger patterns can be generated by stitching multiple frames together.

DFP printing in micrometer resolution can be also achieved using a chromium mask. The chromium masks were fabricated through a typical photolithographic process in a Class 100 cleanroom (Nanohub, Kyoto University). The chromium mask blank (CBL2506Bu-AZP, CST Co., Ltd) features a 100-nm thick chromium layer deposited on a 0.06-inch soda-lime glass substrate, with a proprietary photoresist coating (AZP1350, CST Co., Ltd). The chromium mask fabrication sequentially executes (1) patterning of the chromium mask blank using a microlaser (λ_i: 405 nm, DWL2000, Heidelberg Instruments), (2) development with a tetramethylammonium hydroxide (TMAH, ca. 25% in water) solution using photoresist processing equipment (KD-150CBU, Kanamex Co., Ltd.), (3) etching with a proprietary solution (S-CLEAN S-24, Sasaki Chemical Co., Ltd.), and (4) removing residual material with piranha solution in a wafer spin cleaner (KSC-150CBU, Kanamex Co., Ltd.). The as-fabricated chromium masks were verified to create feature precision as fine as one micrometer.

A graphics design system (GDS) software KLayout (version 0.28.16, https://www.klayout.de/) was used to design the patterns for printing. The software outputs the design in a binary database file format, which is then transferred to the micro-LED and microlaser lithography systems as data input. This applies to both maskless DFP and chromium mask fabrication. Color images were first converted to grayscale with luminance desaturation, then transformed into a two-tone image with Floyd–Steinberg dithering, both using GIMP software (version 2.10.36, https://www.gimp.org/).

Additional details are provided in the captions of the Supplementary Figures.

Results and discussion

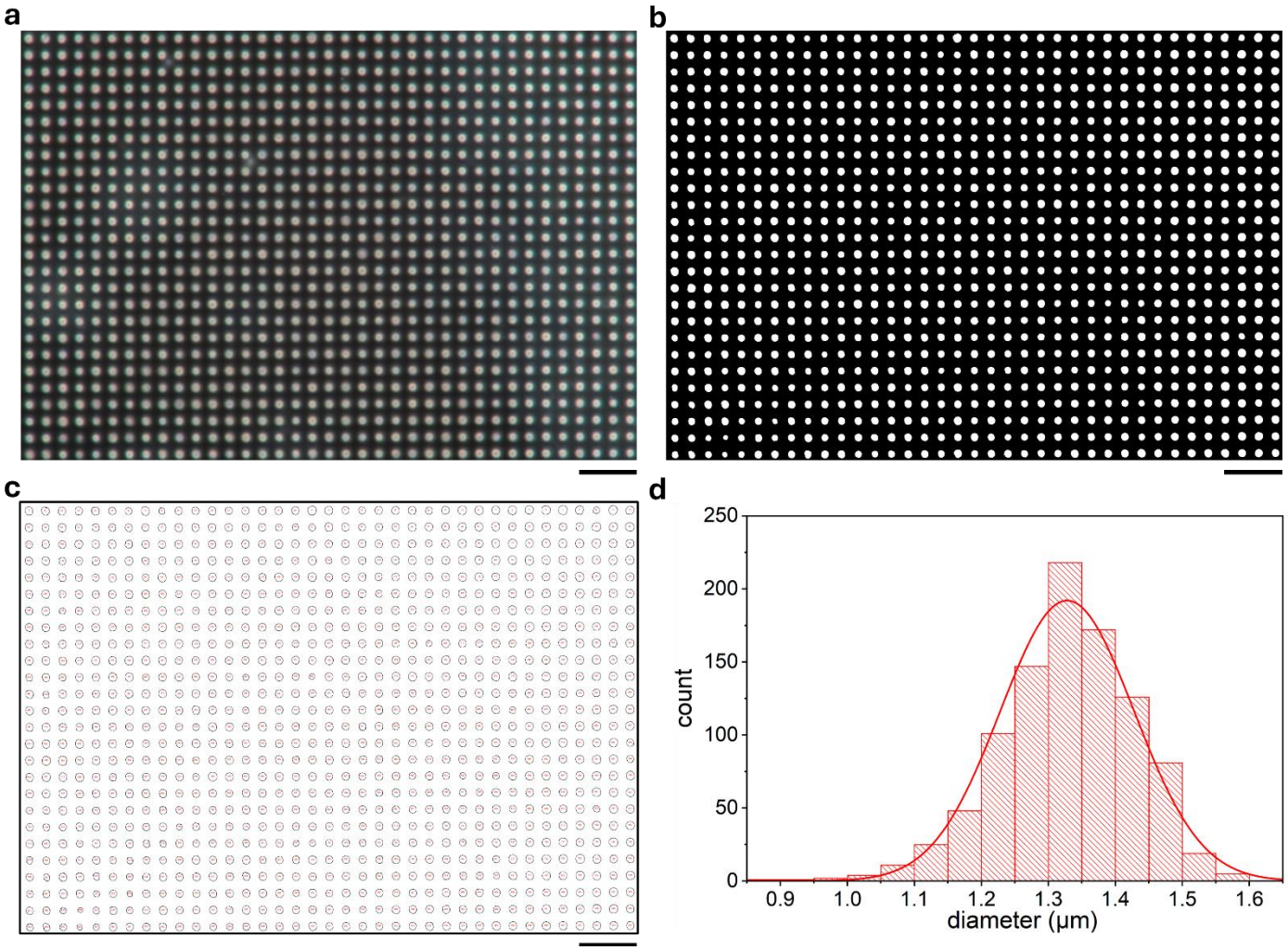

Supplementary Fig. 18 | Resolution of DFP printing. a, Reflective microscopy image taken by a digital stereoscopic microscope (VHX-7000, Keyence). b, The binary image converted from (**a**) by thresholding (ImageJ). **c**, Pixel outlines with index labels obtained from "particle analysis" of (**b**) in ImageJ. **d**, Histogram of dot size distribution with a fitted normal distribution curve, $\mu \pm \sigma = 1.32 \pm 0.10$ μm ($n = 962$). Pixel size is calculated as the equivalent circular diameter from dot area (ImageJ). The mean pixel size (1.32 μm) corresponds to the resolution of 19,240 dots per inch (dpi). Scale bars, 10 μm (**a**–**c**). 2.5-μm-thick PS (192 kDa) film with 9 wt% thioxanthone content relative to PS was cast on cover glass. The film was illuminated using a microLED instrument (λ_i: 405 nm) with an energy dose of 800 J cm^{-2} and developed in 32℃ acetic acid. Same specimen as in Fig. 5e in the main text.

The micro-LED instrument allows pixel-level control of illumination with maximum printing resolution of 25,400 dots per inch (dpi) in principle. With such a microLED system, DFP demonstrates an ultrahigh printing resolution of approximately 20,000 dpi (Supplementary Fig. 18). Whereas the ultimate illumination resolution is diffraction limited and could conceivably reach higher values than 20,000 dpi, the foaming characteristic of DFP features means that adjacent foamed features can interact with each other. Hence, the printing resolution depends on the extent of development when other conditions like polymer/photoinitiator system and UV exposure are kept the same. In practice we observe that pixels set to ≥ 2 μm spacing can retain a distinct flat inter-region between two adjacently foamed features. This was demonstrated with one-dimensional (1D) gratings, consists of 1-μm-width exposed lines and 2-μm-width unexposed lines in the design. As development time increases from 95 s to 5 min (see the figure caption for experimental details),

foam growth is observed for the microprinted lines, while at the same time the length of flat inter-region decreases from 1.6 μm to 0.7 μm. Increasing development time from 5 min to 2 hours observed the inter-region becomes ≤ 0.3 μm (Supplementary Fig. 19).

The resolution is high enough to accurately print diffractive features for visible light. Details of designs are provided in Supplementary Fig. 20 for the DFP specimens with diffractive features and the angle-dependent colours of such a DFP specimen is demonstrated in Supplementary Fig. 21.

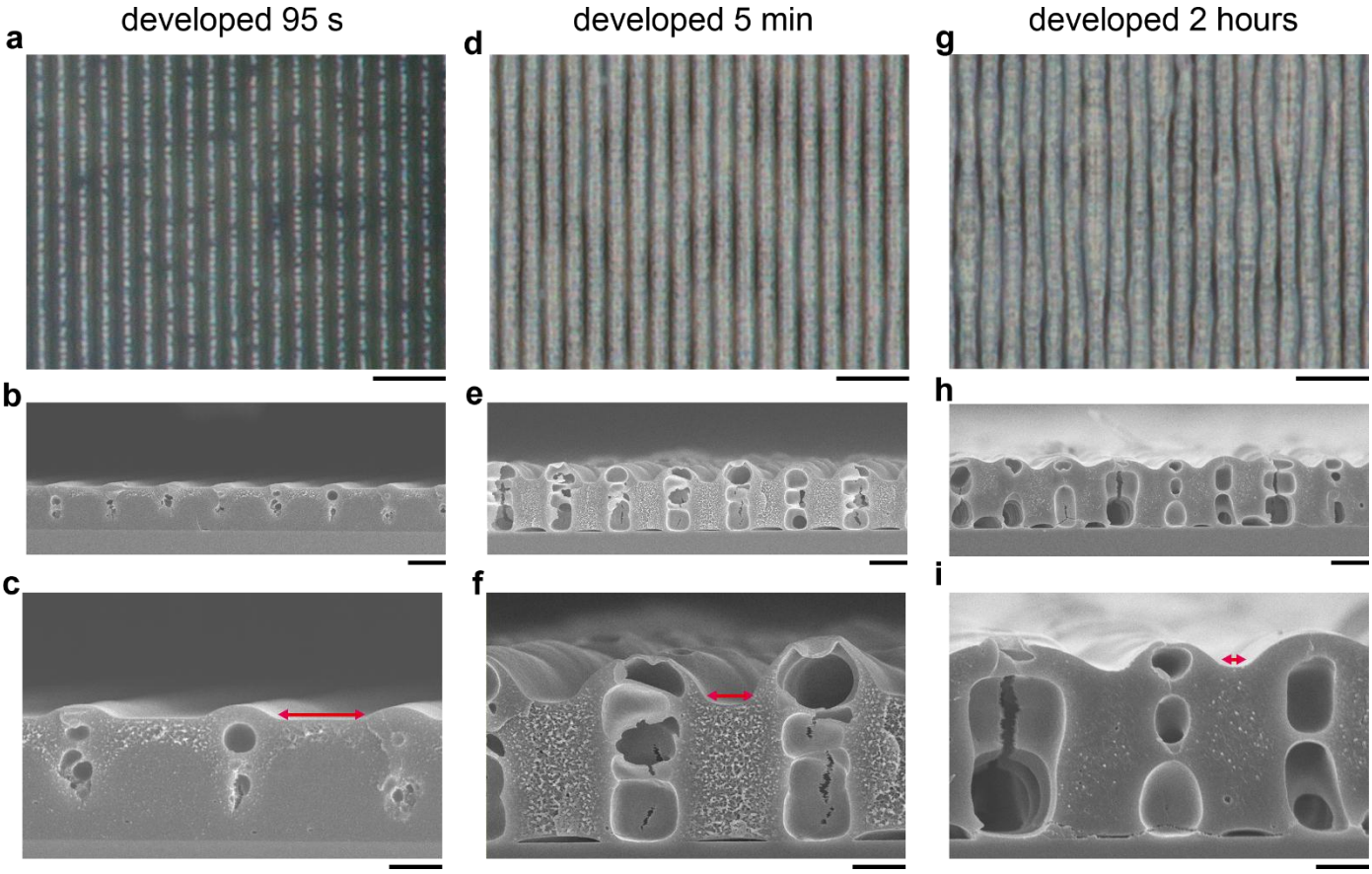

Supplementary Fig. 19 | Dependence of DFP printing resolution on development time. a–**c**, Reflectance microscopy image (**a**), low- and high-magnification SEM images (**b**, **c**) of a printed DFP film developed for 95 s. **d**–**f**, Reflectance microscopy image (**d**), low- and high-magnification SEM images (**e**, **f**) of a printed DFP film developed for 5 min. **g**–**i**, Reflectance microscopy image (**g**), low- and high-magnification SEM images (**h**, **i**) of a printed DFP film developed for 2 hours. Red arrows in (**c**) , (**f**) and (**i**) indicate the flat non-foamed region between two adjacently foamed regions. Scale bars, 10 μm (**a**, **d**, **g**); 5 μm (**b**, **e**, **h**); 1 μm (**c**, **f**, **i**). 2.5-μm-thick PS (192 kDa) film with 9 wt% thioxanthone content relative to PS was cast on cover glass. The film was illuminated using a microLED instrument (λ_i: 405 nm) with an energy dose of 750 J cm^{-2} and developed in 32°C acetic acid. Design of the printing is a one-dimensional (1D) grating composed of 1-μm-width exposed lines and 2-μm-width unexposed lines.

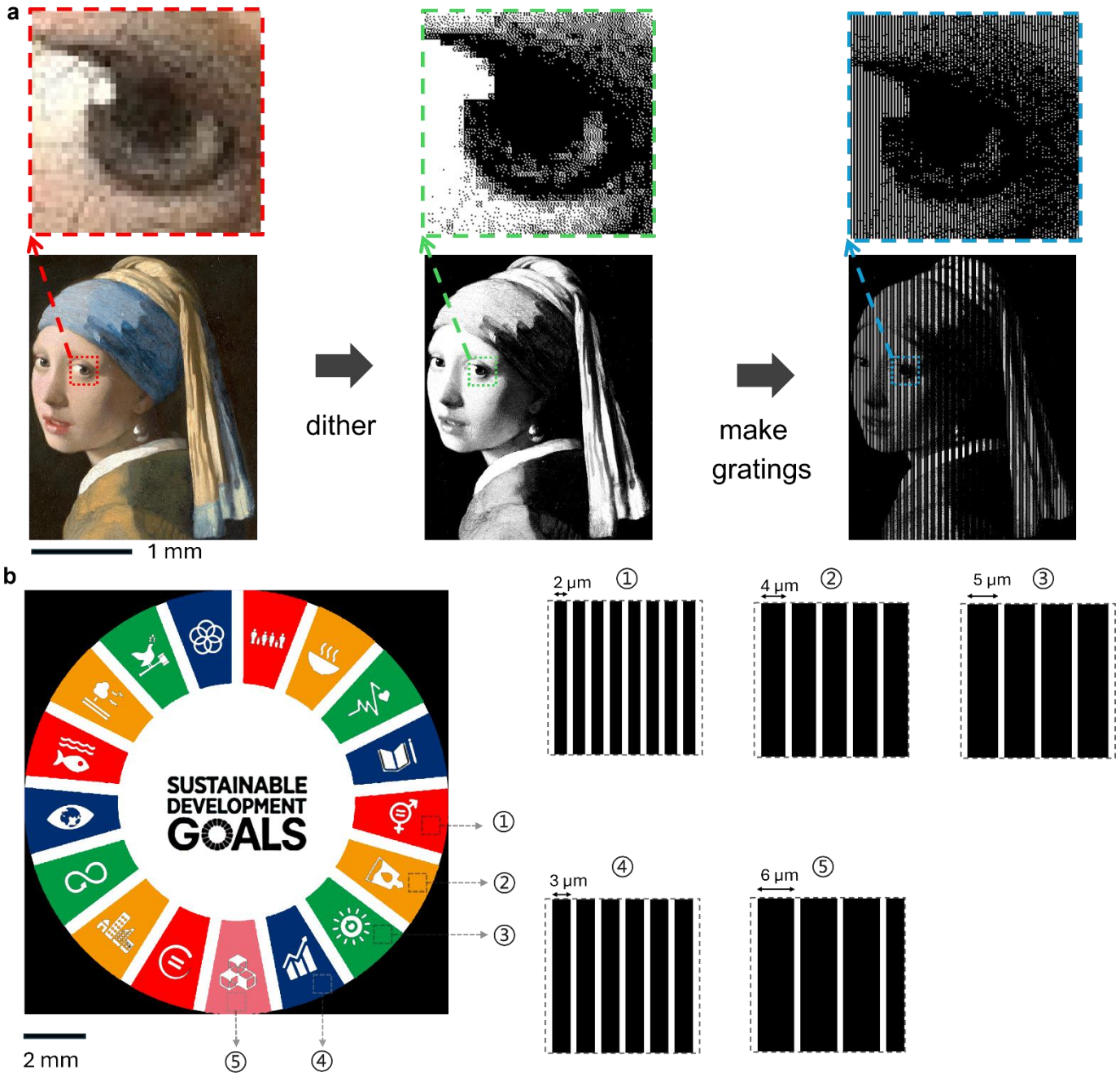

Supplementary Fig. 20 | Pattern design of the DFP specimens with diffraction-induced colors. a, Pattern design of the specimen featuring diffraction-induced colours. The original colour image (Johannes Vermeer's *The Gril with a Pearl Earring*) is converted to a two-tone image with luminance desaturation and Floyd–Steinberg dithering, both using GIMP software (version 2.10.36, https://www.gimp.org/). The two-tone image is further intersected with a periodic grating pattern of 1-μm-width exposed lines and 2-μm-width unexposed lines to generate the final design. White and black colours denote exposed and unexposed regions, respectively. The DFP specimen is created using a microLED illumination. **b**, Pattern design of the specimen with both diffraction-induced colours and structural white. The design is based on the outline of the United Nations Sustainable Development Goals logo. Black and white in the design correspond to the unexposed and exposed regions, respectively. To generate diffractive colours in the sectors, one-dimensional (1D) gratings with 5 different periods are used. These are labelled with different colours in the design. In detail, the unexposed line width is 2 μm for the sectors labelled red (period ①), 4 μm for the sectors labelled yellow (period ②), 5 μm for the sectors labelled green (period ③), 3 μm for the sectors labelled blue (period ④), and 6 μm for the sectors labelled pink (period ⑤), respectively. The width of the exposed lines is 1 μm across all the sectors. A chromium photomask was made using this design. Scale bars, 1 mm (**a**); 2 mm (**b**).

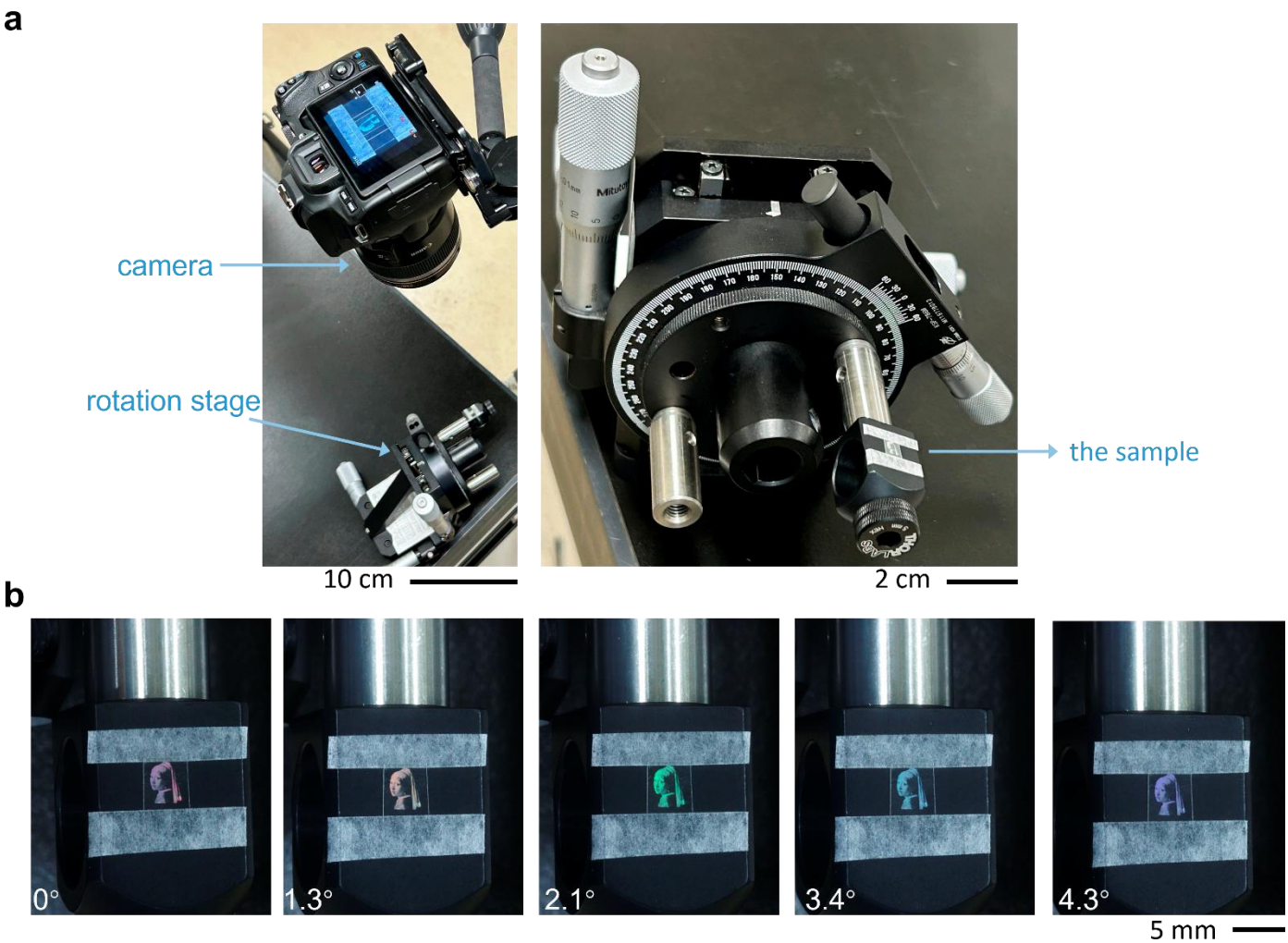

Supplementary Fig. 21 | Angle-dependent colors due to diffraction from a DFP specimen. a, Precision rotation stage for observing diffraction-induced colours. Scale bars, 10 cm (left); 2 cm (right). **b**, A sequence of images was acquired at different rotation angles. The colour, arising from diffraction, continuously shifts from red to violet with increasing rotation angle. All angular values reported here are defined relative to a reference orientation. Scale bar, 5 mm. 2.5-μm-thick PS (192 kDa) film with 9 wt% thioxanthone content relative to PS was cast on PET sheet (Lumirror T60, 188-μm-thick, Toray Industries). The film was illuminated using a microLED instrument (λ_i: 405 nm) with an energy dose of 400 J cm^{-2} and developed in 32°C acetic acid.

Supplementary Note 10

DFP Fibers Prepared via Electrospinning

Method

Polystyrene (PS, 192 kDa) was dissolved in N,N-dimethylformamide (DMF) at a concentration of 35 wt% by stirring at 65°C for 4 h until a clear, homogeneous solution was obtained. After the solution was cooled to room temperature (22±1°C), the photoinitiator (thioxanthone, THX) was added at a THX-to-polymer ratio of 4 wt%, and the mixture was sonicated until a clear solution was obtained. For some printing experiments, a blue dye (Disperse Blue 14) was added to the solution at a dye-to-polymer ratio of 4 wt% prior to sonication.

Polycarbonate (PC) was dissolved in a mixture of tetrahydrofuran (THF): DMF (v/v. 2/1) at a concentration of 20 wt%, stirring at 50°C for 4 h until a clear, homogeneous solution was obtained. After the solution was cooled down to room temperature (22 ± 1°C), the photoinitiator (thioxanthone, THX) was added at a THX-to-polymer ratio of 2 wt%. The mixture was sonicated until a clear solution was obtained.

A schematic of the electrospinning setup is shown in Supplementary Fig. 22. The prepared solutions were electrospun at 16 kV with a flow rate of 2.0 mL h^{-1} under ambient conditions (21℃, 22% relative humidity). The microfibers were collected on a rotating cylindrical collector (diameter: 10 cm, length: 20 cm) at a nozzle-to-collector distance of 15 mm with a rotation speed of 60 rpm. The electrospun mat is ~30 μm in thickness. The electrospun mat was exposed to a light source (λ_i: 385 nm, Thorlabs LEDs for the PS mat and Micro Square LEDs for the PC mat, respectively) with an energy dosage of 1500 J cm^{-2}. The UV-exposed mat was developed in acetic acid at 32℃. The samples were dried immediately using an air blower upon the completion of development.

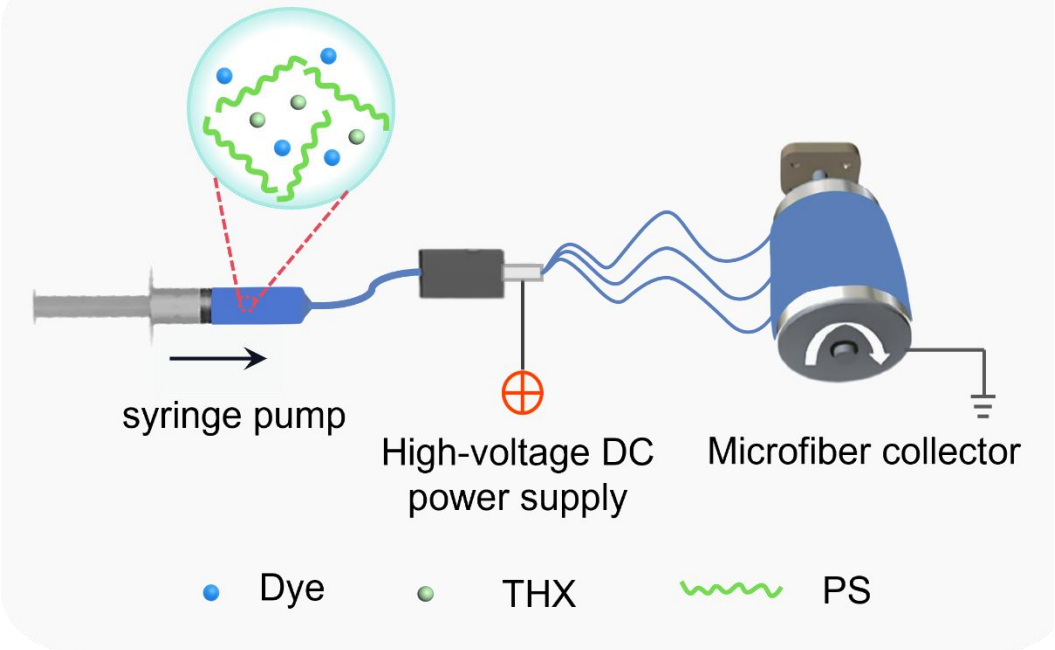

Supplementary Fig. 22 | Schematic diagram of the electrospinning setup.

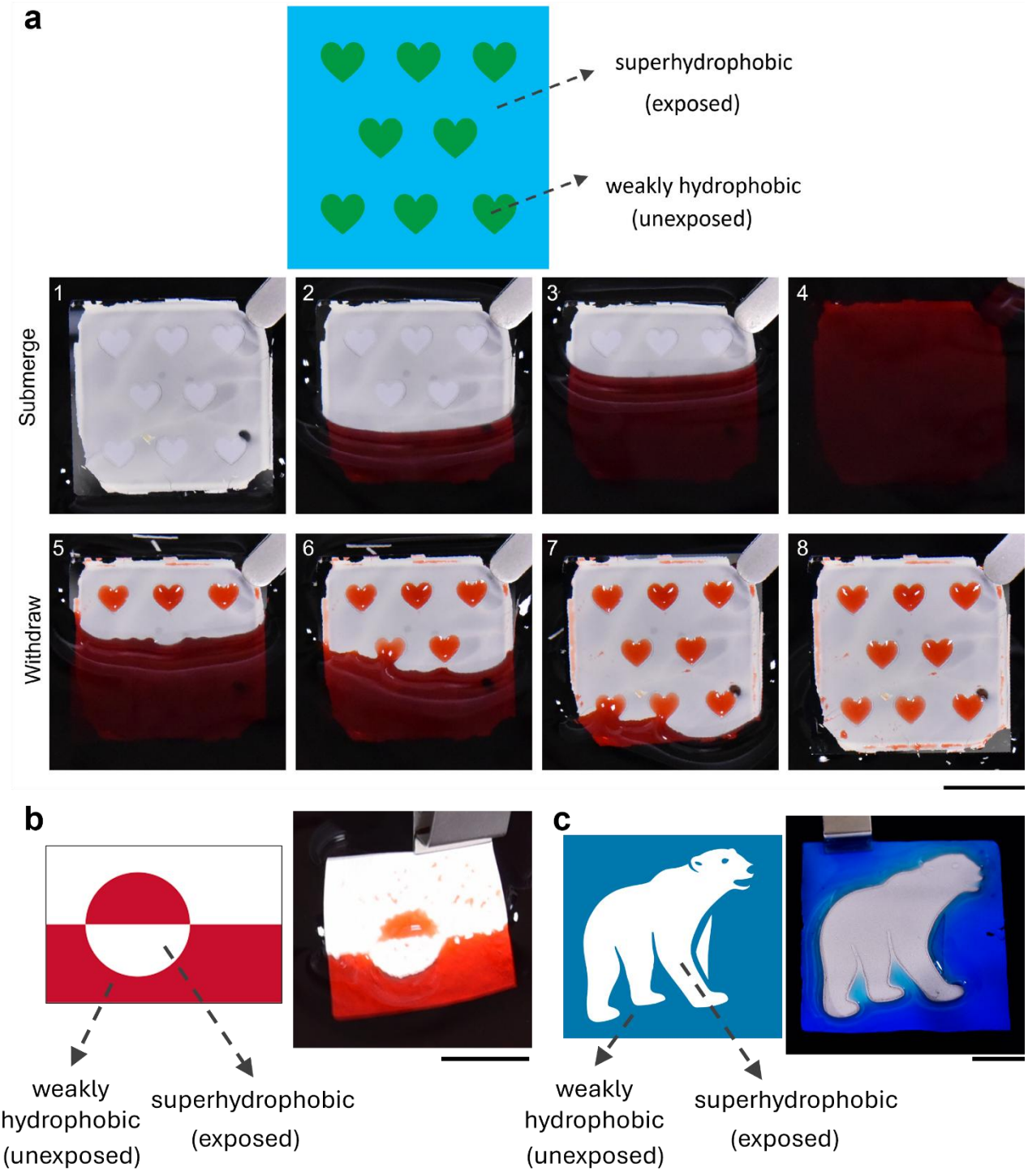

Supplementary Fig. 23 | Patternable water confinement of DFP film and fibrous mats. a, Submerging (labelled 1–4) a DFP film with superhydrophobic patterns in water and then withdrawing it (labelled 5–8). A 4.3-μm-thick polycarbonate (PC) film was spin-cast on silicon wafer using a solution containing 7 wt% thioxanthone (THX) relative to PC. The film was illuminated using a custom LED chamber (Thorlabs λ_i: 385 nm) with an energy dose of 3000 J cm^{-2}. A chromium photomask was used for the patterning. Afterwards, the film was developed in 32°C acetic acid to achieve superhydrophobicity in the exposed regions. The film was submerged in water containing 0.25 wt% Allura Red AC. Upon withdrawal, water was confined to unexposed, weakly hydrophobic regions (the heart-shaped regions). **b**, Lifting a superhydrophobicity-patterned DFP fibrous mat from water (red color from Allura Red AC). The pattern is identical to the Greenland flag. **c**, Lifting a DFP fibrous mat with a different superhydrophobic pattern from water (blue color from Methyl Blue). The pattern is an outline of polar bear. In (**b**) and (**c**), fibrous mats were made by electrospinning the PC solutions containing 2 wt% THX relative to PC. The fibrous mats were illuminated using a LED light source (Micro Square, λ_i: 385 nm) with an energy dose of 1500 J cm^{-2}. Photomasks were made with OHP sheets. The illuminated fibrous mats were developed in 32°C acetic acid to achieve superhydrophobicity in the exposed regions. Scale bars, 10 mm (**a**–**c**).

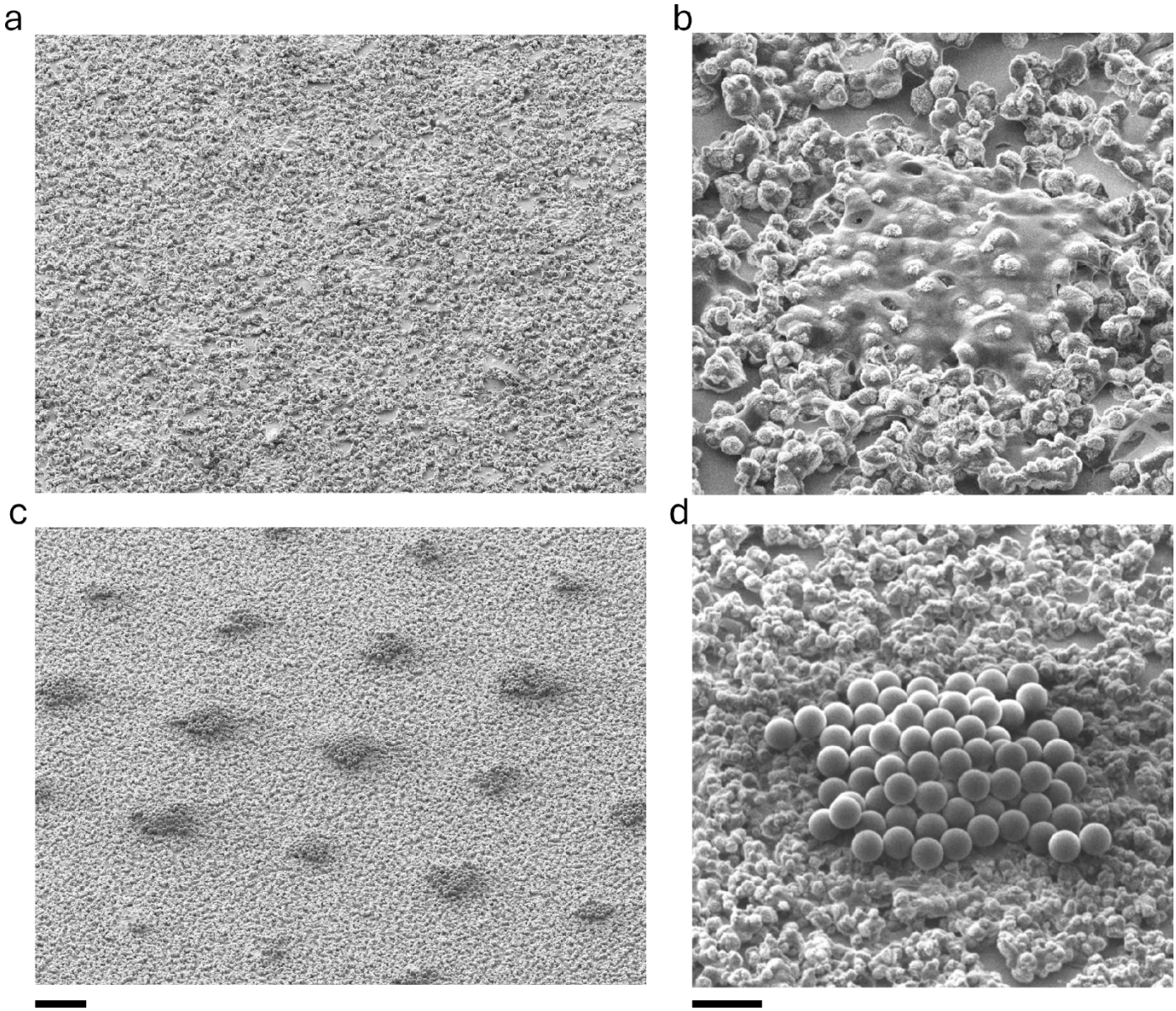

Supplementary Fig. 24 | Pattern-specific capture of microparticles using the liquid confinement effect of DFP. **a**, SEM image of superhydrophobic DFP patterns before contact with the colloidal suspension. **b**, A higher magnification SEM image of (**a**), showing the DFP film is composed of two regions: weakly hydrophobic, skin-preserved (squares), and superhydrophobic, dense microflower surroundings. **c**, SEM image of the superhydrophobic DFP patterns after contact with the colloidal suspension. **d**, Higher magnification SEM image of (**c**), showing specific capture of microparticles in weakly hydrophobic, skin-preserved regions (the squares). **c**, **d** are unprocessed SEM images corresponding to Fig. **6c** and **6d** in the main text, respectively, before colour highlighting. Polymer and photoinitiator are polycarbonate and thioxanthone, respectively, for preparing the film. Scale bars, 100 μm (**a**, **c**); 20 μm (**b**, **d**). Apart from micro-deposition of functional materials, control of vaporisation[14] through factors such as substrate conductivity and local humidity is equally important in applications that require the maintenance of liquid droplets, such as biologicals assays[15-17], and situations that benefit from enhanced evaporation such as environmental cooling[18].

Supplementary Note 11

Preliminary evaluation of the mechanical stability of printed DFP films

Roll-to-roll film and fiber production and in-line photochemical processing are established manufacturing routes, especially within microelectronics, semiconductor and flexible printed optoelectronic industries, where the sequential steps of film casting, exposure, and development are commonly found. One primary difference of the DFP process over classic photolithography is that a mechanical foaming process replaces a chemical etching process to develop structures. Whereas this might slow down overall process times, we have shown, through a study of exposure times, photo-initiator content, polymer molecular weight, and development temperatures that such development processes are thermally, chemically and photo-energetically tunable, and can be optimized further according to specific industrial needs. A short report of various durability tests of DFP printed films including a preliminary observation of fracture modes; demonstrations of scalability (to A3 size) and printing uniformity, and examples of material combinations are provided (Supplementary Notes 11–13 and Supplementary Figs. 25–29). Whilst such preliminary tests proved encouraging, limitations will ultimately depend on the uniformity of process control parameters of all steps at the industrial scale.

Method

1. Sample preparation

Mechanical stability of printed DFP films was evaluated by cyclic thermal shock and bending. The primary stable foam developed in this study was a 192-kDa PS film, which was printed in a decorative Mandala pattern, similar to the bending example given in Extended Data Figs. 8f, g. As for sample preparation, 2.5-μm-thick PS films were prepared by spin-casting a solution in which thioxanthone (THX) was added at 7 wt% relative to the polymer. The substrate was a PET sheet (Lumirror T60, 100-μm-thick, Toray Industries). The films were illuminated in an LED chamber (Thorlabs, λ_i: 385 nm) with an energy dose of 600 J cm-2, while an OHP mask was placed on the film for photopatterning. The illuminated films were developed in acetic acid at room temperature (22 ℃) for 1 min.

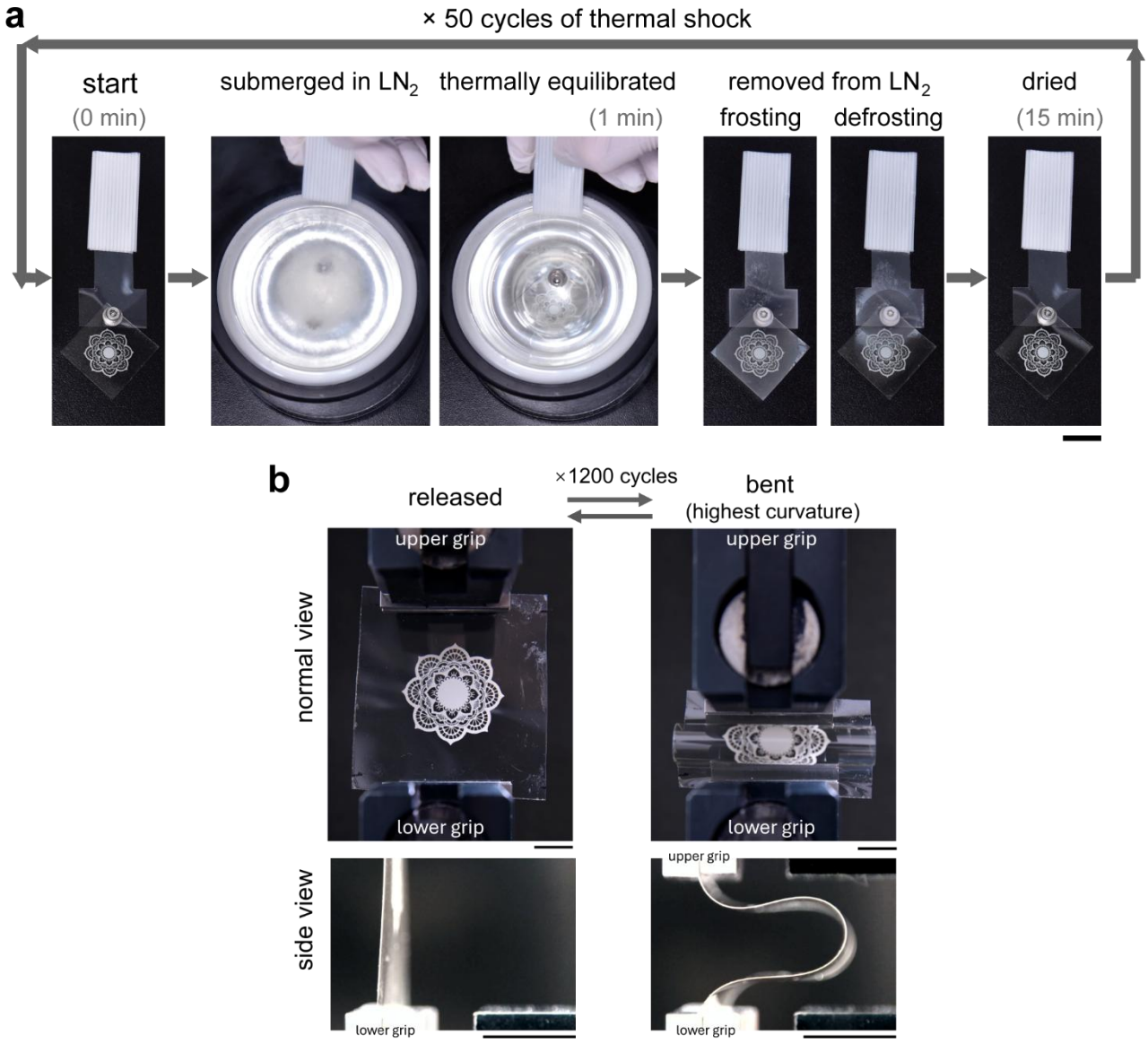

Supplementary Fig. 25 | Evaluation of mechanical stability. a, Photographs showing the cyclic thermal shock using liquid nitrogen. **b**, Photographs showing the cyclic bending test. Scale bars, 2 cm (**a**); 1 cm (**b**).

2. Cyclic thermal shock

A 36 mm × 36 mm specimen of printed DFP film was immersed in liquid nitrogen (LN_2) and held for 1 min to reach thermal equilibrium. The sample was then removed from LN_2 and exposed to ambient air (~40% RH) for 14 min to return to room temperature. During this period, surface frosting and subsequent defrosting were observed. This cycle was repeated 50 times in total, as illustrated in Supplementary Fig. 25a.

3. Cyclic bending

A specimen of printed DFP film (50 mm × 50 mm) was clamped between two grips (5 mm clamping length at each end), with the lower grip fixed and the upper grip displaced downward by a preset displacement of 25 mm and subsequently released to impose cyclic bending deformation, using a tensile testing machine (STA-1150, Orientec Co., Ltd., Tokyo, Japan). This displacement corresponded to a maximum curvature of 0.26 mm^{-1}, while the measured maximum force reached 0.37 N. To be comparative to current literature[19] the bending test was carried out at a frequency of 7.5 cycles per minute for a total of 1200 cycles. During bending, the deformation of the film was simultaneously observed using two cameras: a DSLR camera (EOS Kiss X10, Canon) was positioned normal to the film surface, and a digital camera (XW200, Shenzhen Hayear Electronics, China) was positioned along the lateral direction to record curvature changes. The cyclic bending is demonstrated in Supplementary Fig. 25b.

4. Characterization

To quantify any significant changes in the internal microstructure of the DFP film, direct transmittance spectrum was taken using a UV–Vis spectrometer (MCPD-3700, Otsuka Electronics) over different cycles of the thermal shock or bending test. The transmittance spectra were numerically integrated over the wavelength range of 320–820 nm based on the trapezoidal rule for quantitative comparison (Equations S17).

$$I = \sum_{i=1}^{n-1} \frac{T_{D,i} + T_{D,i+1}}{2} (\lambda_{i+1} - \lambda_i) \quad \text{(S17)}$$

where λ_i and $T_{D,i}$ denote the wavelength and corresponding direct transmittance at i-th data point, respectively, n is the total number of data points within the integration range, and I is the integrated intensity over the specified wavelength range. Relative change in the integrated intensity was evaluated by Equation S18.

$$\frac{I_j - I_0}{I_0} \times 100\% \quad \text{(S18)}$$

where I_0 and I_j are the integrated spectral intensities of the initial state and that after j-th cyclic test of thermal shock or bending, respectively.

Surface SEM images were taken for a control printed DFP film (no bending, no thermal shock), the printed film after 50th thermal shock, and the printed film after the 1200th bending, using a JEOL JSM-7500F unit at an acceleration voltage of 5 kV. The microstructural changes in the DFP film induced by bending were also analyzed using FIB–SEM (Focused Ion Beam–Scanning Electron Microscope). Clean

cross-sections of the specimen after the 1200th bending were obtained through FIB treatment. The FIB–SEM images were taken using Carl ZEISS (Crossbeam 540) under an accelerating voltage of 2.0 kV.

Results and discussion

1. Results and discussion: Cyclic thermal shock

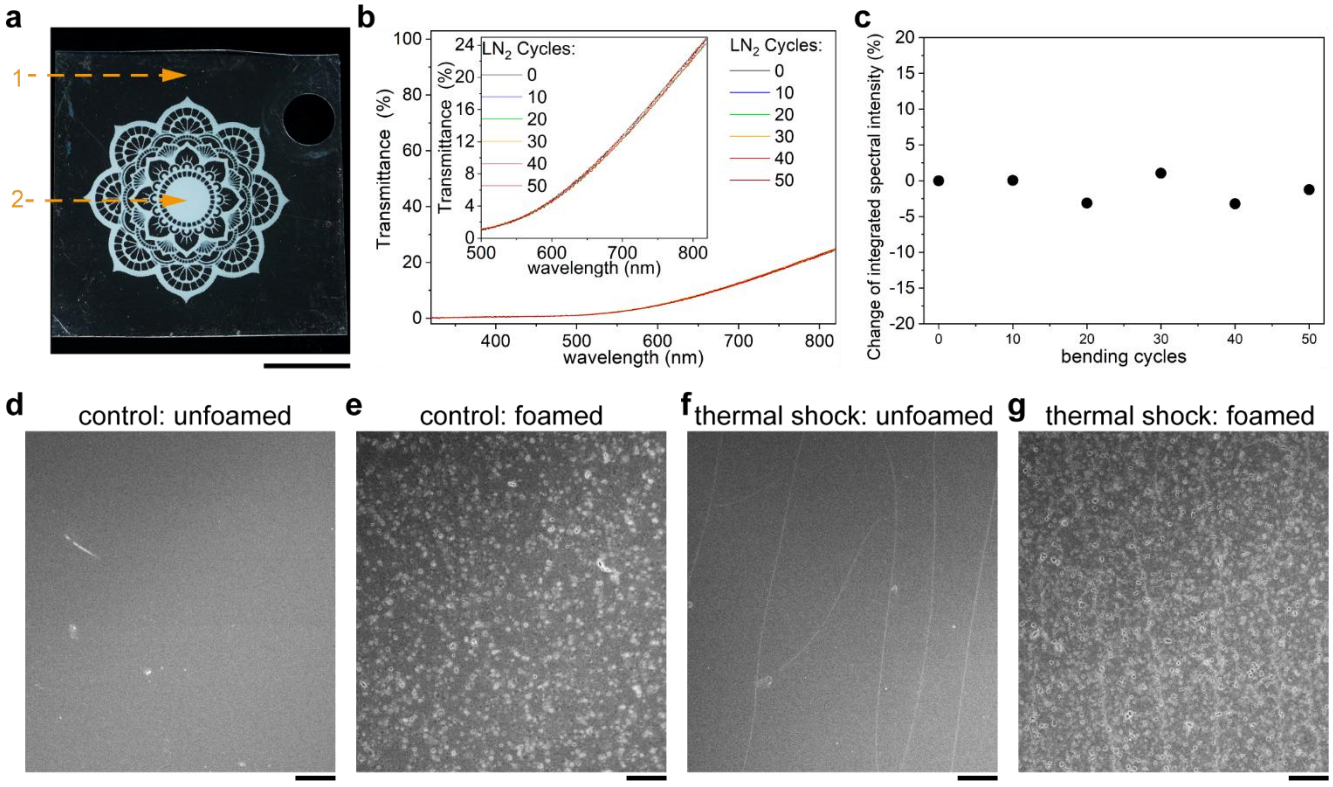

Supplementary Fig. 26 | Cyclic thermal shock. a, The printed DFP film after 50 cycles of thermal shock using liquid nitrogen. The labels "1" and "2" denote the unfoamed region and foamed region, respectively, for SEM observations. **b**, Direct transmittance spectra over different cycles of thermal shock (inset: magnified view). The spectra were measured at the central foamed region, label "2" in (**a**). **c**, Relative change in the integrated intensity of direct transmittance over different cycles of thermal shock. **d**, Surface SEM image of the unfoamed region of a control printed DFP film. **e**, Surface SEM image of the foamed region of a control printed DFP film. **f**, Surface SEM image of the unfoamed region (label "1" in **a**) of the printed DFP film after 50 cycles of thermal shock. **g**, Surface SEM image of the foamed region (label "2" in **a**) of the printed DFP film after 50 cycles of thermal shock. Scale bars, 1 cm (**a**); 10 μm (**d**–**g**).

The impact of cyclic thermal shock on the structures and properties of printed DFP film was studied at both macroscopic and microscopic levels (Supplementary Fig. 26). Overall, the printed pattern remained intact after repeated cycling of thermal shock and no discernible changes were observed at the macroscopic level, as shown in Supplementary Figs. 25a and 26a. Direct transmittance spectra of the foamed region were monitored over different cycles of thermal shock (Supplementary Fig. 26c). The change in the integrated intensity of direct transmittance was less than 3%, which indicates the nanostructures of the foam could be largely preserved.

For comparison purposes, a printed DFP film was prepared, and its surface was observed using SEM for both unfoamed and foamed regions, without cyclic thermal shock. Supplementary Figs. 26d show that the unfoamed region of the control DFP film is free of any cracks. Supplementary Figs. 26e show that foamed

region of the control sample has characteristic surface-adjacent pores. Supplementary Fig. 26f, g reveals the impact of cyclic thermal shock on the morphology of printed DFP film at the microscopic level. Comparing the figures, cyclic thermal shock generates straight extended cracks with lengths in the unfoamed region of the film. The same cracks appear in the foamed regions, but have a more tortuous character, indicating the effect of the underlying porous foam in preventing the straight crack propagation normally seen in homogenous matter.

2. Results and discussion: Cyclic bending

The impact of cyclic bending on the structures and properties of printed DFP film was also studied at both macroscopic and microscopic levels (Supplementary Fig. 27). The intricate foamed pattern is preserved after 1200 cycles of acute bending. However, stress whitening is observed at the location of maximum curvature in the unfoamed region (label "1" in Supplementary Fig. 27a).

Direct transmittance spectra of the foamed region were monitored over different cycles of bending (Supplementary Fig. 27b). The variation of integrated spectral intensity was less 3.5 % (Supplementary Fig. 27c), which is consistent with absence of noticeable changes in the foamed region at the macroscopic level.

SEM images reveal the impact of cyclic bending on the structures of the unfoamed and foamed DFP film at the microscopic level. As shown in Supplementary Fig. 27d, straight cracks with a spacing of ~15 μm were observed at the surface of the unfoamed region after 1200 cycles of bending, which explains the stress whitening phenomenon at the location of maximum curvature (label "1" in Supplementary Fig. 27a). A cross-section of the unfoamed film shows the thin ~2.5 μm PS film on top of the thicker 100 μm PET; note the slight scattering contrast. This upper surface was under tensile stress during bending. The cracks visible from surface SEM, are also present throughout the depth of the film. We speculate that the crack may have originated at the interface of the PET and PS surface, propagating both inwards and outwards from that point, resulting in a crack-tip at the PS film surface (Supplementary Figs. 27e, f). In the case of foamed DFP films, SEM surface microscopy also reveals the presence of cracks (Supplementary Fig 27g), albeit with a similar diffuse and meandering appearance that was also seen in the case of thermal-shock treated samples (Supplementary Figs. 26g). In cross-section, these samples show that cracks, which may also have originated at the PS/PET interface, fail to consistently propagate to the surface, becoming pinned by the porous bubbles (Supplementary Figs. 27h, i). This incomplete crack propagation leads to the diffuse appearance of the surface SEM (Supplementary Figs. 27g).

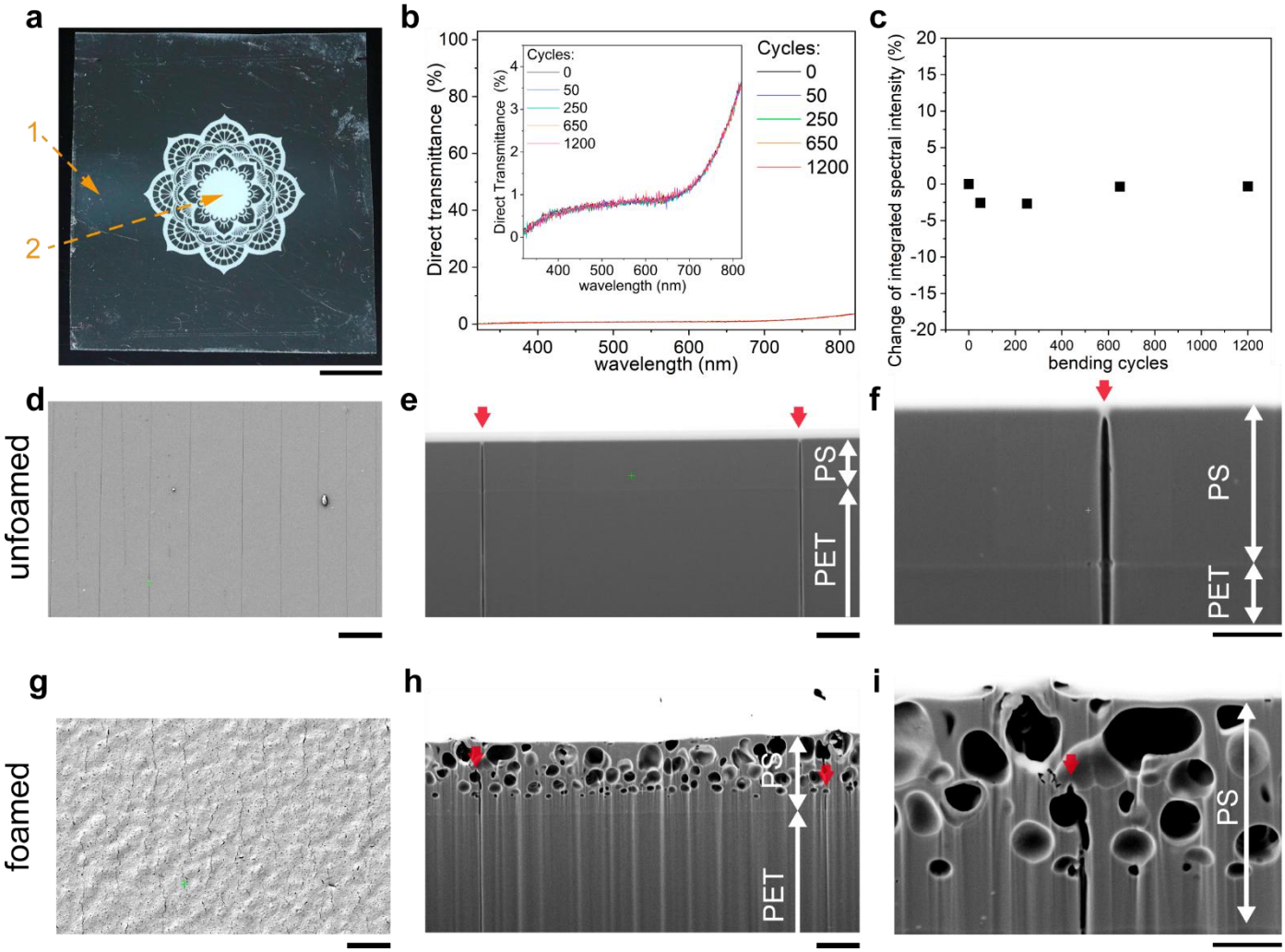

Supplementary Fig. 27 | Cyclic bending. a, The printed DFP film after 1200 cycles of bending. The labels "1" and "2" denote the unfoamed region and foamed region at the location of maximum curvature, respectively, for SEM observations. **b**, Direct transmittance spectra over different cycles of bending (inset: magnified view). The spectra were measured at the central foamed region, label "2" in (**a**). **c**, Relative change in the integrated intensity of direct transmittance over different cycles of bending. **d**, Surface SEM image of the unfoamed region (label "1", where stress whitening is observed) after 1200 cycles of bending. **e**, Cross-sectional image of the unfoamed region (label "1", where stress whitening is observed) after 1200 cycles of bending, obtained by FIB-SEM. **f**, High magnification image of (**e**). **g**, Surface SEM image of the foamed region (label "2") after 1200 cycles of bending. **h**, Cross-sectional image of the foamed region (label "2") after 1200 cycles of bending, obtained by FIB-SEM. **i**, High magnification image of (**h**). Red arrow in (**e**, **f**, **h**, **i**) indicates an end of the extended cracks. Scale bars, 1 cm (**a**); 20 μm (**d**, **g**); 2 μm (**e**, **h**); 1 μm (**f**, **i**).

3. Overall conclusion and recommendations.

Using 192-kDa polystyrene as the model, the preliminary study on mechanical stability indicates that the printed DFP pattern can be preserved after cyclic thermal shock using liquid nitrogen or acute bending. Negligible changes are observed after the cyclic tests at the macroscopic level, which is also verified by the <3.5% variation in the integrated intensity of direct transmittance. Such variances in transmittance are significantly smaller than those observed during large area coatings of DFP surfaces. However, at the microscopic level, extended cracks are formed in both unfoamed and foamed regions of the printed DFP films by cyclic thermal shock or bending. The porous structure formed by foaming is found to dull the propagation of cracks both in plane and through the thickness of the film.

While beyond the scope of this paper, further investigation of the specific mechanisms behind crack propagation in this composite, porous system would necessitate deeper understanding of film-film interaction, internal stress distributions, and identification of the mechanisms behind failure in both materials[20,21]. A future study would also explore the phenomenon of mechanical failure in DFP foams more systematically, using multiple polymers and molecular weights, and where necessary with additives to counter any negative mechanical failures.

Supplementary Note 12

Commentary on the feasibility of industrial scalability and printing uniformity

Whilst the largest films in the main figures were prepared by a batch-process method, commonly found in the semi-conductor industry, of polymer photoresist spin-coating, illumination under a physical mask, and wet-development by a solvent, we demonstrated that the DFP method can be extended to continuous printing processes.

Method

Polystyrene (PS, 192 kDa) was primarily used for evaluating scale-up feasibility. PS was dissolved in chloroform to make 10–15 wt% solution and thioxanthone (THX) was added to the solution in the amount of 4–7 wt% relative to PS. Film coatings were performed using an RK K101 Control Coater with a No. 3 bar (24 μm wet thickness) at 2 m min^{-1}. The substrate is PET sheet (Lumirror T60, 188-μm-thick, Toray Industries, Japan) unless otherwise specified. The film was illuminated using a large LED arrary (Micro Square Co., Ltd, λ_i: 385 nm). Energy dose is in the range of 300–900 J cm^{-2} and a lower energy dosage is needed for the DFP printing with a higher THX-to-PS ratio. The illuminated film was developed in acetic acid at 32℃ for 1 to 10 min. The film was dried immediately upon the completion of development using an air blower bulb. Supplementary Fig. 28 shows the scale-up process. Supplementary Table 3 compares the experimental conditions between spin-cast small DFP samples and bar-coated large samples.

Uniformity of DFP printing was studied using 192-kDa polystyrene (PS) and THX. The concentration of polystyrene solution was 9 wt%. Except for this, the other conditions for bar-coating were kept the same as mentioned above. The film was illuminated using a large LED array (Micro Square Co., Ltd, λ_i: 385 nm) with an energy dose of 150 J cm^{-2}. The illuminated film was developed in acetic acid at 32℃ for 1 min. For evaluating uniformity, a pattern of circular dots in A4 size was printed.

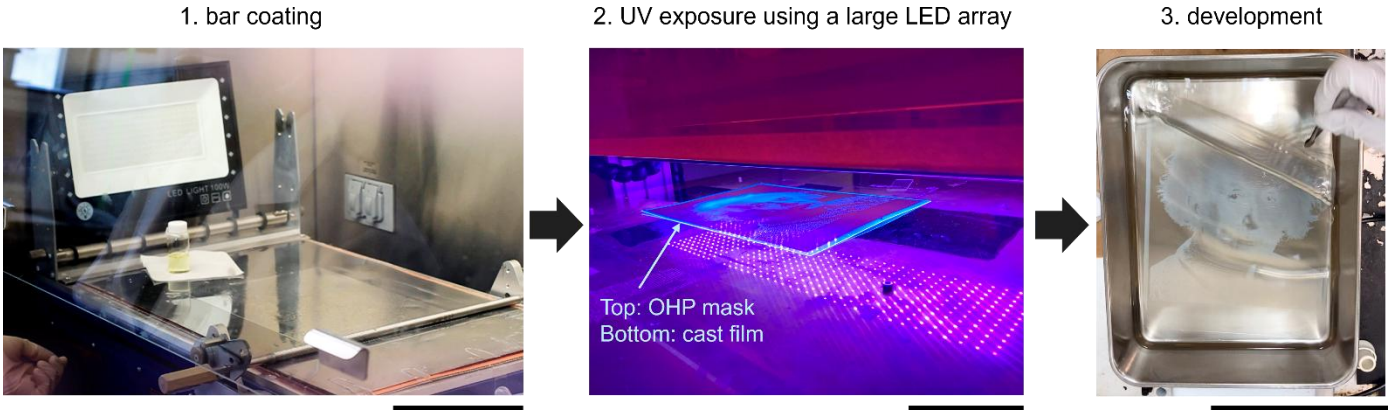

Supplementary Fig. 28 | Photographs showing the scale-up process. Photographs from left to right: bar-coating a polymer/photoinitiator solution on A4 PET sheet (left), UV illumination using the large LED array (Micro Square Co., Ltd) (middle), and retrieving a developed DFP film from the solvent tank (right). Scale bars, 20 cm.

Table 3| Experimental conditions for making small-sized and large-sized DFP samples.

	Small-sized samples (area ⩽10 cm ×10 cm)	Large-sized samples (area >10 cm ×10 cm)
Substrate	glass (primarily)	PET or PP sheet
Film preparation	Spin-casting: able to create 100 cm^2 films in 30s	Bar-coating: able to create A3 (~ 1260 cm^2) films in 10 s
Illumination	Custom LED chamber (Thorlabs, λ_i = 340, 365, 375, 385, 405 nm, power: ~0.03 W/cm^{-2} at 10 cm working distance)	Industrial scale, narrow bandgap LED array (Thorlabs, λ_i = 365, 385, and 405 nm, power: as high as 0.75 W/cm^{-2} at 10 cm working distance)
Development	Immersion in small glass dish	Immersion in a large tank
Drying	Manually, using air blower bulb	Manually, using an air blower bulb

Results and discussion

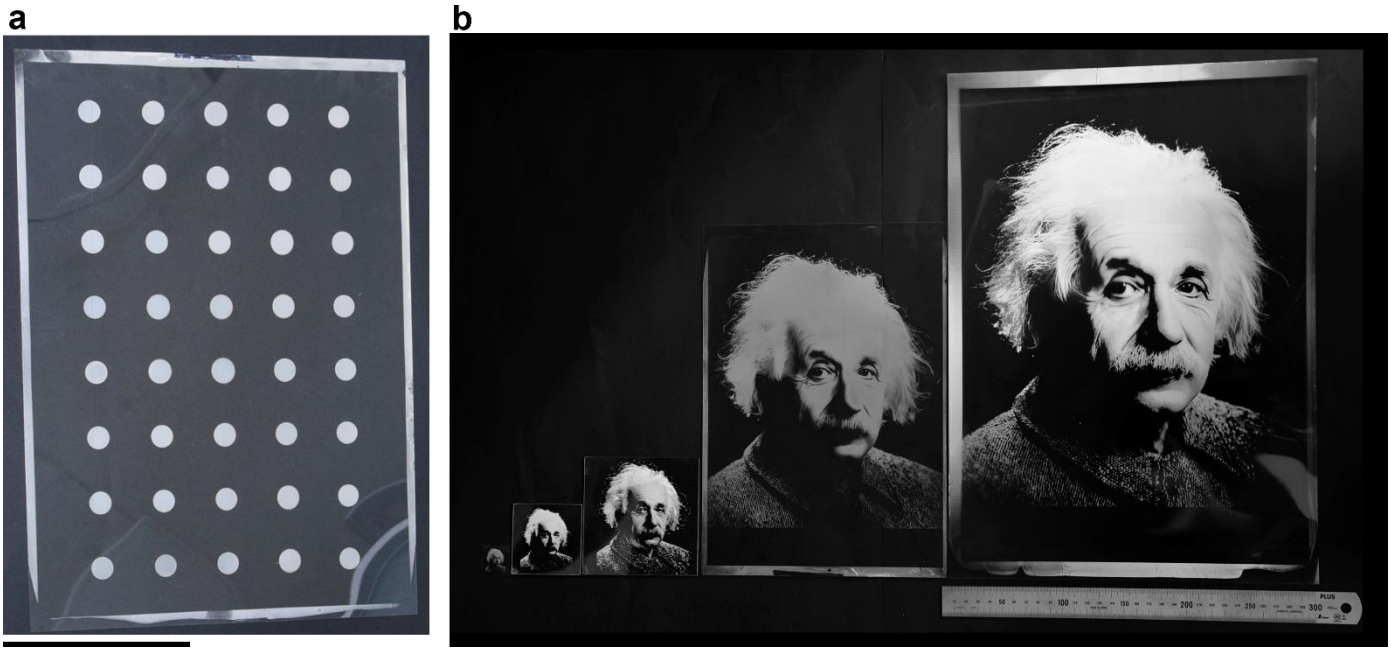

Supplementary Fig. 29 | Scale-up demonstration of the DFP process and test of print uniformity. a, Photograph of A4 printing of circular dots. Scale bar, 10 cm. The PS/THX film was illuminated using a large LED array (Micro Square Co., Ltd, λ_i: 385 nm) with an energy dose of 150 J cm^{-2}. The illuminated film was developed at 32°C acetic acid for 1 min. **b**, Scale-up printing of the photo Albert Eistein (Original photo by Oren Jack Turner, Princeton, N.J.), where the samples ≤ 10 cm × 10 cm were made by spin casting and illuminated using a UV projector (λ_i: 405 nm) or using custom LED chamber (Thorlabs, λ_i: 405 or 385 nm), while the samples > 10 cm × 10 cm were made by bar coating and illuminated using a large LED array (Micro Square Co., Ltd, , λ_i: 385 nm). The substrate for A4 and A3 specimen is 188-μm-thick PET sheet (Lumirror T60, Toray Industries, Japan) and OHP film (0.1-mm-thick polyester film, Sakae Technical Paper Co., Ltd., Japan), respectively. Ruler for scale (cm).

As a preliminary study on the uniformity of the DFP printing at large size, we prepared a 192-kDa polystyrene film in A4 dimensions using thioxanthone. Supplementary Fig 29a shows the printing of a chart of 8×5 circular dots, in a single, unoptimized trial. The printed whiteness is visually uniform from dots to dots throughout the A4 specimen. Moreover, we demonstrated the scaling up of DFP printing by more than

an order of magnitude in area from a 2.4 cm×2.4 cm square on glass to an A3 size on PET sheet (Supplementary Fig 29b). Here, the “Einstein” photo is also a good example showing grayscale printing of DFP process: regions with stronger illumination intensity can be developed to make a more foamed structure, and hence stronger whiteness (see Fig. 5a in the main text for schematic illustration). The use of a high-power UV-A light source also reduces the illumination time from hours to minutes. Here, A3-size printing is made with polystyrene and thioxanthone, using an OHP film (0.1-mm-thick polyester film, Sakae Technical Paper Co., Ltd., Japan) as the substrate for the bar coating. More work is recommended in future to systematically optimize the experimental conditions for scale-up studies and to promote the translation of DFP technology from laboratory research to industrial-scale application.

Supplementary Note 13

Commentary on use of other polymers and photoinitiators

DFP is primarily demonstrated using polystyrene (PS) in this study. Mechanistic studies of DFP reveals that its formation primarily depends on plasticity of the photo-sensitized polymer, weak solvent induced phase separation, and hypotonic permeation. Photoinduced crosslinking between hydrogen abstraction–induced radical sites, and beta scission in the presence of oxygen are common mechanisms to a wide range of commercial polymers. Hence, we show that DFP process is also broadly applicable to a range of commercially available polymers (Extended Data Fig. 6). We demonstrated DFP in widely used commodity polymers including polyethylene terephthalate (PET) and poly(methyl methacrylate) (PMMA). We note that in examples like PMMA, with poor sensitivity to UV-A exposure, the addition of a photoinitiator is essential[22,23]. We studied how to harness the recrystallization behaviour of polycarbonate (PC), a tough transparent engineering plastic, for patternable control of surface hydrophobicity. We also demonstrated DFP in polysulfone (PSU), a thermally and chemically stable high-performance plastic, and in cellulose triacetate (CTA), a bio-based material with high optical clarity.

We have also realized formation of DFP structures via a diverse set of photoinitiators. Thioxanthone is the primary photoinitiator studied in this paper. Apart from it, we note benzophenone and its derivatives e.g., 2-methylbenzophenone, 4,4′-bis-(diethylamino)-benzophenone, etc., anthraquinone, and phenanthrenequinone are possible for DFP processes. These photoinitiators have a broad absorption window in the wavelength range of 300–400 nm. Supplementary Table 4 summarizes the polymers and photoinitiators studied in this paper.

Table 4 | Polymers and photoinitiators investigated in this study

Polymer			Photoinitiator		
	Supplier	Remarks		Supplier	Remarks
PS	Sigma Aldrich	primarily used (Figs 1–3, 5, etc.)	THX	TCI	primarily used (Figs 1a, 2–6, etc.)
PET	Tsukasa Pecto	demonstrated (Extended Data Fig. 6)	MBP	TCI	Demonstrated (Fig. 1b)
PMMA	Sigma Aldrich	demonstrated (Extended Data Fig. 6)	BP	Sigma Aldrich	For BP, BDABP, AQ, and PQ, observed DFP formation in proof-of-concept experiment with PS. Hence, note they are possible for DFP processes.
PC	Sigma Aldrich	demonstrated (Figs 4 & 6, etc.)	BDABP	Sigma Aldrich	
PSU	Sigma Aldrich	demonstrated (Extended Data Fig. 6)	AQ	TCI	
CTA	Fujifilm Wako	demonstrated (Extended Data Fig. 6)	PQ	TCI	

Note: PS denotes polystyrene, PET denotes polyethylene terephthalate, PMMA denotes poly(methyl methacrylate), PC denotes polycarbonate, PSU denotes polysulfone, CTA denotes cellulose triacetate, THX denotes thioxanthone, MBP denotes 2-methyl benzophenone, BP denotes benzophenone, BDABP denotes 4,4′-bis-(diethylamino)-benzophenone. AQ denotes anthraquinone, PQ denotes phenanthrenequinone, and TCI denotes Tokyo Chemical Industry.

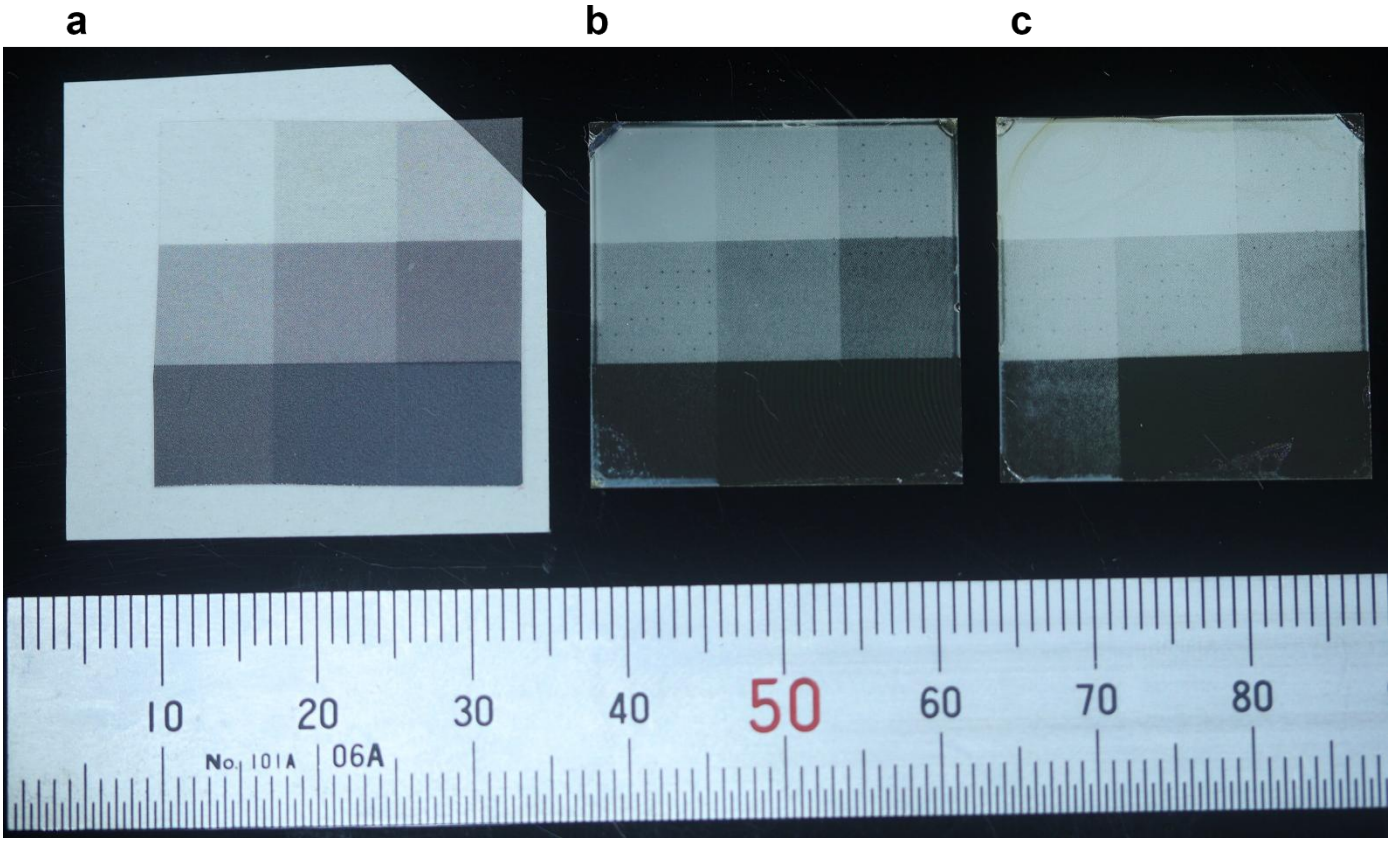

Supplementary Fig. 30 | Effect of different drying methods. **a**, Greyscale overhead projector (OHP) mask (background is a piece of A4 paper for contrast). **b**, DFP film dried using an air blower immediately upon the completion of development. **c**, DFP film dried via natural solvent evaporation. Ruler for scale (cm). 2.5-μm-thick polystyrene (192 kDa) was spin-cast on cover glass using a solution containing 7 wt% of thioxanthone relative to polymer. The film was illuminated using a custom LED chamber (Thorlabs λ_i: 385 nm) with an energy dose of 500 J cm^{-2}. A greyscale OHP sheet consisting of a 3×3 grid display is used as the photomask: an 8-bit greyscale gradient ascending from 0 (bottom-right) to 255 (top-left) in uniform numerical increments. The illuminated films were developed in 32℃ acetic acid for 20 s. The sample dried via natural solvent evaporation is opaquer than one dried immediately using an air blower. This result indicates the effect of drying on the resultant DFP films: the longer the developer (acetic acid) remains in the film, the more development continues to happen.

Supplementary Video Legends

Supplementary Video 1 | Serial cross-sectional images taken by FIB-SEM. The images were taken by repeatedly etching the DFP sample with a focused ion beam while imaging it with SEM (Crossbeam 540, Carl ZEISS). This DFP sample was prepared under standard conditions at the development time of 25 s.

Supplementary Video 2 | The bubble-isolated 3D structural models based on FIB-SEM analysis. The FIB-SEM image stack was reconstructed into a three-dimensional (3D) volume using the software Dragonfly 3D World ZEISS edition (Version 2025.1). Spatial segmentation of the reconstructed 3D volumes was performed using the machine learning model (Pre-trained U-Net Depth=5) implemented in the software. The segmented bubbles were used to determine their centroid positions and volume-equivalent diameters. This video shows the segmented bubbles and the glass substrate.

Supplementary Video 3 | of a collapsed DFP film. The hydrophobicity of a collapsed polycarbonate DFP film is strong enough that a water droplet forced into contact with the surface by a micro-controlled dispenser does not detach from the needle.

Supplementary Video 4 | Microscale liquid isolation onto unexposed regions of DFP film with superhydrophobic patterns. A water droplet passed over a DFP film with superhydrophobic patterns detaches small volumes from the main droplet, forming isolated liquid domains on the unexposed, weakly hydrophobic regions.

Supplementary References

1. El-Kashef, H. The necessary requirements imposed on polar dielectric laser dye solvents. *Physica B* **279**, 295-301 (2000).
2. Hori, K., Matsuno, H. & Tanaka, K. Sorption kinetics of methanol in thin poly(methyl methacrylate) films studied by optical reflectivity. *Soft Matter* **7**, 10319-10326 (2011).
3. Nikitas, N. F., Gkizis, P. L. & Kokotos, C. G. Thioxanthone: a powerful photocatalyst for organic reactions. *Org. Biomol. Chem.* **19**, 5237-5253 (2021).
4. Torikai, A., Hattori, T. & Eguchi, T. Wavelength effect on the photoinduced reaction of polymethylmethacrylate. *J. Polym. Sci. Pol. Chem.* **33**, 1867-1871 (1995).
5. Nikitas, N. F., Skolia, E., Gkizis, P. L., Triandafillidi, I. & Kokotos, C. G. Photochemical aerobic upcycling of polystyrene plastics to commodity chemicals using anthraquinone as the photocatalyst. *Green Chem.* **25**, 4750-4759 (2023).
6. Vera, M. U. & Durian, D. J. Angular distribution of diffusely transmitted light. *Phys. Rev. E* **53**, 3215-3224 (1996).
7. Gibson, I. & Ashby, M. F. The mechanics of three-dimensional cellular materials. *Proceedings of the royal society of London. A. Mathematical and physical sciences* **382**, 43-59 (1982).
8. Yanagisawa, N., Tani, M. & Kurita, R. Dynamics and mechanism of liquid film collapse in a foam. *Soft Matter* **17**, 1738–1745 (2021).
9. Larson, R. G. The Structure and Rheology of Complex Fluids. (Oxford University Press, 1998).
10. Song, J., Holten-Andersen, N. & McKinley, G. H. Non-Maxwellian viscoelastic stress relaxations in soft matter. *Soft Matter* **19**, 7885–7906 (2023).
11. Cui, Y. H., Paxson, A. T., Smyth, K. M. & Varanasi, K. K. Hierarchical polymeric textures via solvent-induced phase transformation: A single-step production of large-area superhydrophobic surfaces. *Colloid Surf. A-Physicochem. Eng. Asp.* **394**, 8-13 (2012).
12. Ye, Y. S. & Choi, K. Y. Preparation of Micron-Sized Spherulitic Bisphenol A Polycarbonate Particles in Thin Films. *Macromol. Mater. Eng.* **294**, 847-854 (2009).
13. Feng, L. et al. Super-hydrophobic surfaces: From natural to artificial. *Adv. Mater*. **14**, 1857-1860 (2002).
14. Talbot, E. L., Berson, A., Brown, P. S. & Bain, C. D. Evaporation of picoliter droplets on surfaces with a range of wettabilities and thermal conductivities. Phys. Rev. E 85, 061604 (2012).
15. Gayathri, R., Kar, S., Nagai, M., Mahapatra, P. S. & Santra, T. S. Massively Parallel High-Throughput Single-Cell Patterning and Large Biomolecular Delivery in Mammalian Cells Using Light Pulses. Small 19, (2023).
16. Ekblad, T. & Liedberg, B. Protein adsorption and surface patterning. Current Opinion in Colloid and Interface Science vol. 15 499–509 Preprint at https://doi.org/10.1016/j.cocis.2010.07.008 (2010).
17. Delamarche, E., Pereiro, I., Kashyap, A. & Kaigala, G. V. Biopatterning: The Art of Patterning Biomolecules on Surfaces. Langmuir 37, 9637–9651 (2021).

18. Bin Nadeem, T., Imran, M., Tandis, E. & Arshad, A. Surface engineering and nanomaterials for sustainable indirect evaporative cooling systems. npj Thermal Science and Engineering 1, 1 (2026).
19. Kishino, M., Hisano, K., Kishimoto, Y., Taguchi, R. & Shishido, A. Bending Fatigue Analysis of Various Polymer Films by Real-Time Monitoring of the Radius of Curvature and Heat Generation. *J. Phys. Chem. C* **127**, 14510-14517 (2023).
20. Marsavina, L. & Linul, E. Fracture toughness of rigid polymeric foams: A review. *Fatigue Fract. Eng. Mater. Struct.* **43**, 2483-2514 (2020).
21. Thouless, M. D., Li, Z., Douville, N. J. & Takayama, S. Periodic cracking of films supported on compliant substrates. *J. Mech. Phys. Solids* **59**, 1927-1937 (2011).
22. Mita, I., Obata, K. & Horie, K. Photoinitiated Thermal Degradation of Polymers II. Poly(methyl methacrylate). Polym. J. 22, 397–410 (1990).
23. Carbaugh, D. J., Wright, J. T., Parthiban, R. & Rahman, F. Photolithography with polymethyl methacrylate (PMMA). Semicond. Sci. Technol. 31, 025010 (2016).